공학석사 학위논문

Seismic Performance Evaluation of the High-Rise Building Using Nonlinear Analysis

비선형 해석을 통한 초고층 건물의 내진성능 평가

2017 년 8 월

서울대학교 대학원

건축학과

정 승 용

Abstract

Seismic Performance Evaluation of the High-Rise Building Using Nonlinear Analysis

Jeong, Seung Yong
Department of Architecture and Architectural Engineering
College of Engineering
Seoul National University

A core wall system is commonly used as a lateral-load-resisting system of a high-rise building. The use of coupled shear walls connected by coupling beams is necessary due to the presence of openings at the core walls. Generally coupling beams yield prior to shear walls under seismic actions, because the beams are designed much weaker than the walls. Likewise, the cyclic behavior of coupling beam elements significantly affects the energy dissipation characteristics of a core wall system. In this study, the seismic performance evaluation of a high-rise building with core wall system is carried out by performing a series of nonlinear static and dynamic analyses using ETABS 2016. The nonlinear time history analyses are conducted using seven earthquake records at each of Design Basis Earthquake (DBE) and Maximum Considered Earthquake (MCE) levels. And the results of seismic performance evaluations by nonlinear static procedure and time history analyses are compared. The responses of the high-rise building according to

the modeling methods of the basement and the characteristics of earthquake records are also studied.

Based on the analysis results, the coefficient method suggested by ASCE 41-13 nonlinear static analysis procedure generally overestimates the seismic performance of the high-rise building compared to the nonlinear time history analysis. The responses above the ground level are similar regardless of the basement modeling methods, but there are large differences below the ground level depending on the basement models. The responses of nonlinear time history analysis are very sensitive depending on the characteristics of ground motions. Because of the influence of the higher modes, the results of the nonlinear time history analysis largely differ from those of the nonlinear static analysis.

Keywords : Seismic Performance, High-Rise Building, Nonlinear Dynamic Analysis, Basement, Coupling Beam

Student Number : 2015-22850

Contents

List of Tables

List of Figures

Chapter 1. Introduction

1.1 Introduction

Generally the strength design of a high-rise building in Korea is governed by the wind loads rather than seismic loads. However, the seismic design of a high-rise building based on the codes using linear analysis may be inappropriate to understand the actual behavior under seismic actions, because the general codes such as KBC 2016 and ASCE 7-10 are established mainly for the low-to-mid rise buildings. As it is inefficient to design a building to remain in the elastic range under seismic loads, the strength reduction factor, *R*, is used considering ductility of the structural system in the codes. It is difficult to predict the actual ductility of the system under seismic load, and the seismic loads based on *R* factor may be inaccurate. Thus, seismic performance evaluation of tall buildings by performing nonlinear analysis is needed.

In this study, the seismic performance evaluation of a high-rise building with building frame system planned in Seoul is conducted. The building was designed by a structural design company using the linear analysis based on the KBC 2016. Since the building has a height of 199.9 m, the design of the building was governed by wind loads which were determined by wind tunnel tests. The seismic design code of KBC 2016 is based on the design basis earthquake (DBE) which is defined as the earthquake with 475-year return periods. Considering the importance of high-rise buildings, a more conservative seismic design procedure may be required, and the accurate evaluation of the performance is also required. Thus, seismic performance evaluation of the building using nonlinear static and nonlinear time history analyses is conducted. In order to check the seismic performance under rare earthquakes, the nonlinear time history analyses are also conducted using

maximum considered earthquakes.

The building has the massive core walls to resist wind loads, and the core walls are connected by coupling beams. The coupling beams are expected to yield prior to vertical members, because generally the beams are designed weaker than the vertical members to achieve ductile behavior of the system. And core walls may remain elastic even under severe seismic loads due to the thickness of 1,200 mm. Thus, the inelastic hysteretic behavior of coupling beams affects the energy dissipation of the system substantially.

1.2 Scope and objectives

The main purpose of this study is to evaluate the seismic performance of the high-rise building with the coupled core walls and coupling beams by using nonlinear static and dynamic analyses. The nonlinear modeling of the coupling beams is also intensively studied, because the coupling beams are the most vulnerable members in the system. The seismic performance evaluation using nonlinear static procedure may not represent the actual behavior of a high-rise building due to large effects of higher order modes. For better understanding of such effects, the seismic performance evaluations based on both nonlinear static analysis procedure and nonlinear dynamic analysis are compared.

1.3 Organization

This thesis consists of seven main chapters. The introduction of the study is briefly shown in Chapter 1. The literature reviews of the design code and guidelines for performance-based seismic design, and the studies about coupling beams are shown in Chapter 2. Chapter 3 consists of the information of analysis models and nonlinear modeling approach for the building. The DBE and MCE ground motions used for nonlinear time history analysis are shown in Chapter 4. The results of the nonlinear static analyses and seismic performance evaluation are shown in Chapter 5. The results of the nonlinear time history analyses and seismic performance evaluation and the findings associated with the results are shown in Chapter 6. The conclusion is summarized in Chapter 7.

Chapter 2. Literature Review

2.1 Design codes and guidelines

2.1.1 Korean design codes and guidelines

Design projects using performance-based seismic design are becoming frequent. Considering the current trend, the contents about performance-based seismic design have been added in KBC 2016, which permits to design a building based on various performance objectives using nonlinear analysis when it is difficult to apply the design coefficients and factors of KBC 2016. **Table 2-1** shows the performance objectives suggested by KBC 2016.

Table 2-1 Performance objective in KBC 2016

Seismic use group	Performance objective	
	Performance level	Seismic hazard
S	Operational (or immediate occupancy)	1.0 times design effective ground acceleration
	Life safety & collapse prevention	1.5 times design effective ground acceleration
1	Life safety	1.2 times design effective ground acceleration
	Collapse prevention	1.5 times design effective ground acceleration
2	Life safety	1.0 times design effective ground acceleration
	Collapse prevention	1.5 times design effective ground acceleration

The seismic performance should be evaluated using both nonlinear static and nonlinear dynamic analysis in KBC 2016. However, KBC 2016 does not suggest detailed procedures of nonlinear analysis.

The Architectural Institute of Korea published the Guidelines for

Performance-Based Seismic Design of Residential Buildings (2015). This guideline is based on the FEMA 440 (2013) and ASCE 41-13 (2014), and has the similar procedures of design. However, the modeling parameters are revised based on the condition of Korean industry, and are generally more conservative. In the guideline, the performance evaluation can be conducted by both of the nonlinear static analysis and nonlinear dynamic analysis.

The performance evaluation of nonlinear static analysis procedure is based on the equivalent linearization method in FEMA 440. The performance of a building is evaluated by the state of global system and individual members at the performance point. And the maximum interstory drift is limited to 1.5%.

More than seven ground motions are scaled to be used for nonlinear dynamic analysis so that the average spectra of ground motions are not less than 90% of 1.3 times the target spectra. The performance evaluation is conducted by the average responses of ground motions. The same interstory drift limit of nonlinear static analysis procedure is used for the evaluation of the system. The individual members are evaluated by dividing into the deformation-controlled and force-controlled members, which is the same as ASCE 41-13.

2.1.2 ASCE 41-13

ASCE 41-13 is one of the most widely used guidelines for nonlinear analysis and seismic performance evaluation. It consists of the nonlinear modeling and the evaluation of performance level, suggesting the backbone curves of members for inelastic modeling. The acceptance criteria for shear walls and coupling beams are given by their plastic chord rotations. However, the modeling of hysteretic behavior is not suggested in this guideline.

The seismic performance evaluation using nonlinear static analysis procedure is suggested in ASCE 41-13. The effective fundamental period is determined by the idealized force-displacement curve from the pushover curve of nonlinear static analysis. With the modification factors to reflect multi-degree-of-freedom behavior, load distributions and hysteretic behavior, a target displacement is determined. The seismic performance of global system and individual members is evaluated when the lateral displacement of a building is at the target displacement. The procedures for nonlinear dynamic analysis are also presented in the guideline. The seismic performance in nonlinear dynamic analysis is directly evaluated by the responses of a series of ground motions.

2.1.3 PEER/ATC 72-1

The PEER/ATC 72-1 is specialized in the nonlinear modeling of a high-rise building. It suggests the modeling methods of coupling beams in tall buildings. From the guideline, the coupling beams with span-to-depth ratio lager than 2 are dominated by flexure. And the effective stiffness of coupling beams is suggested as $0.15EI_g$ which is much lower than the effective stiffness of general beams suggested by ACI 318-14 or ASCE 41-13. From PEER/ATC 72-1, the acceptance criteria of coupling beams in ASCE 41-13 are conservative compared to the observation of experiments.

PEER/ATC 72-1 also reviews the response of core walls in the high-rise building under seismic loads. The followings are the findings for core wall behavior in a high-rise building.

1) The variation of effective shear stiffness of core walls does not affect largely the shear and moment force of core walls above the ground level.

2) The elastic model can be used for the shear walls expected not to yield.

3) The strains of core walls at the upper part of a building should be limited to low tensile strains, twice the yield strain, to avoid excessive nonlinear deformation at the upper part.

4) Reducing longitudinal reinforcement over the height has a little effect on the reduction of maximum shear force and moment over the height of walls

2.1.4 Guidelines for Performance-Based Seismic Design of Tall Buildings (TBI 2017)

The Guidelines for Performance-Based Seismic Design of Tall Buildings (TBI 2017) focuses on the design practice and seismic performance evaluation of a high-rise building. This guideline suggests modeling parameters which are generally not included in other guidelines, such as the modeling of basement and detailed effective stiffnesses for concrete members.

In this guideline, the seismic performance evaluation is conducted for the service level earthquake and maximum considered earthquake. The service level earthquake is defined as an earthquake with return period of 43 years, and the maximum considered earthquake is defined as an earthquake with return period of 2475 years. For the seismic performance evaluation under a service level earthquake, a linear-elastic model is used, and a nonlinear model also can be used. The response spectrum analysis and linear time history analysis are used for the linear model. The story drift is limited as 0.5% under the service level earthquake. The nonlinear time history analysis using more than 11 ground motion records is recommended for the performance evaluation of the maximum considered earthquake. The peak transient story drift ratio is limited to 4.5%, and the residual story drift ratio is limited to 1.5% under the maximum considered earthquake.

2.2 Previous studies

Tall buildings have massive core walls connected by relatively weak coupling beams. The coupling beams are expected to yield prior to vertical members under seismic loads, so the inelastic modeling of coupling beams is the most important for tall buildings. The guidelines for nonlinear analysis such as ASCE 41-13 do not offer the modeling of hysteretic behavior of coupling beams. Therefore, there is no choice but to depend on the experiment results of previous studies.

2.2.1 Xiao et al. (1999)

The hysteretic behavior of coupling beams without diagonal reinforcement depending on the span-to-depth ratio and the arrangement of longitudinal reinforcement is studied in the paper. Focused on the specimens with span-to-depth ratio of 4 which are shown in **Figure 2-1**, the experiment results are shown in **Figure 2-2**.

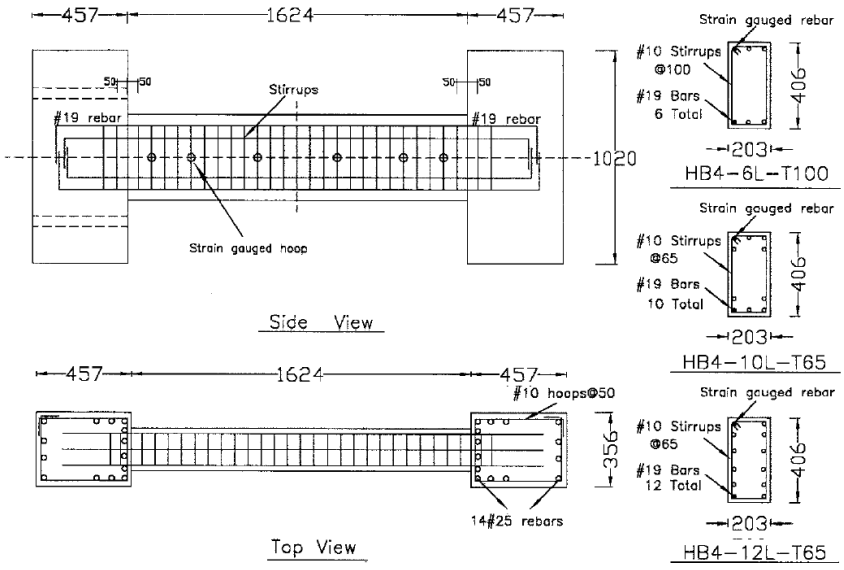

Figure 2-1 Specimen with span-to-depth ratio of 4 tested by Xiao et al. (1999)

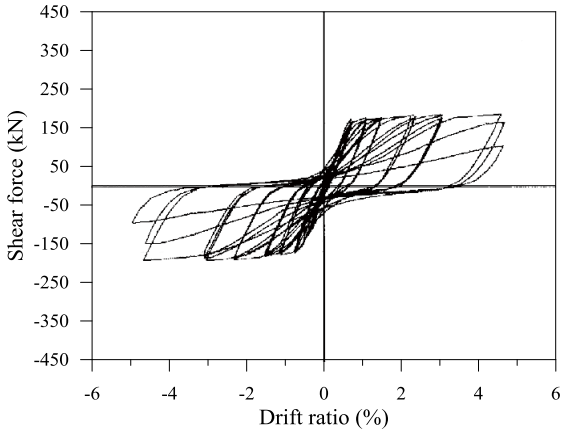

(a) HB4-6L-T100

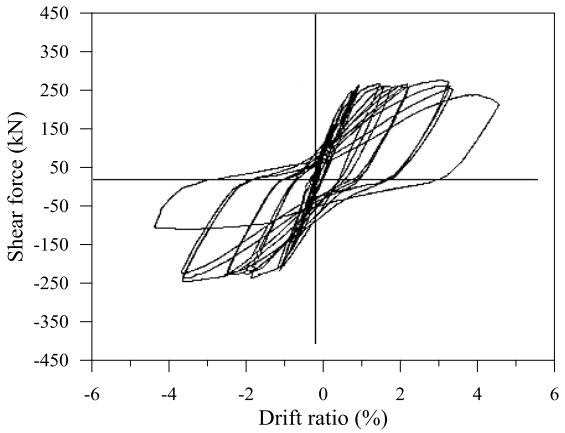

(b) HB4-10L-T65

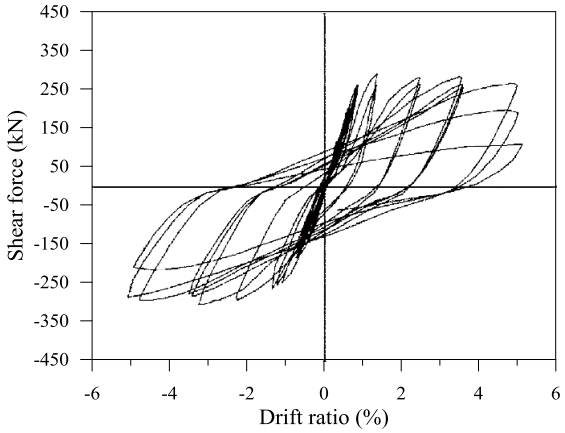

(c) HB4-12L-T65

Figure 2-2 Experimental results of HB4 specimens (Xiao et al., 1999)

The reinforced concrete (RC) coupling beams with conventional longitudinal reinforcement failed due to the end of the beam, and the strength development was delayed due to the crack closing time during reloading after the concrete crack occurred at the end. The pinching effect was affected by the amount and arrangement of flexural bars. The specimen of HB4-12L-T65 having distributed flexural reinforcement showed larger energy dissipation and ductility. As shown in **Figure 2-3**, the span-to-depth ratio of the coupling beam influenced the maximum plastic rotation.

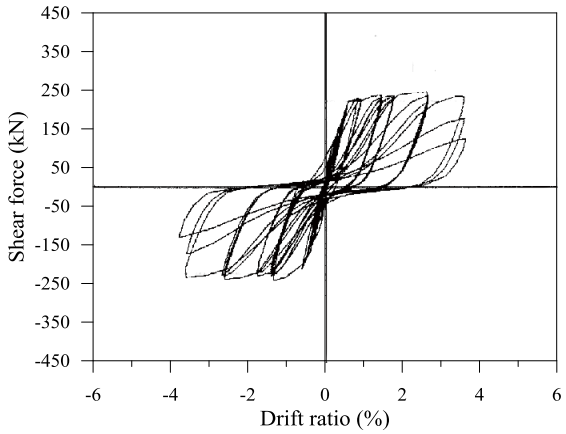

(a) HB3-6L-T100

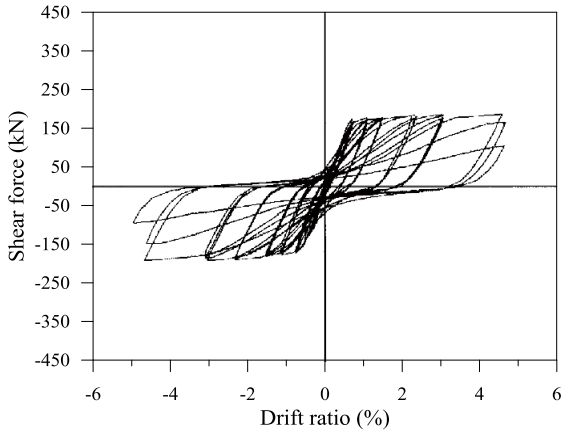

(b) HB4-6L-T100

Figure 2-3 Comparison of experimental results with span-to-depth ratios of 3 and 4 (Xiao et al., 1999)

2.2.2 Naish et al. (2013)

The hysteretic behavior of coupling beams with diagonal reinforcement depending on the details of conforming transverse reinforcement and the span-to-depth ratio were studied in the paper. The diagonal confinement in ACI 318-05 and the full section confinement in ACI 318-08 were compared. The specimens with the span-to-depth ratio of 2.4 and 3.3 were tested. Also the specimen with conventional longitudinal reinforcement and span-to-depth ratio of 3.3, FB33 specimen, was also tested. Focused on the FB33 specimen shown in **Figure 2-4**, the experiment results are shown in **Figure 2-5**.

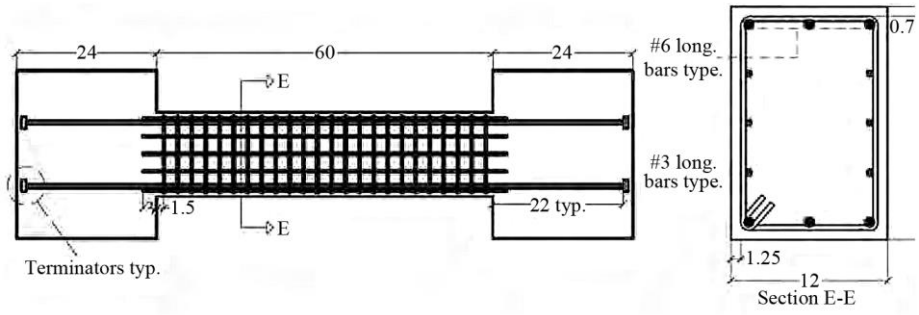

Figure 2-4 FB33 specimen tested by Naish et al. (2013)

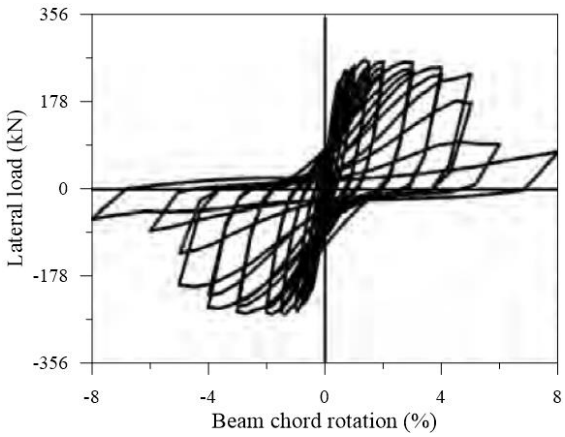

Figure 2-5 Experimental result of FB33 specimen (Naish et al., 2013)

According to the experiment results, the full section confinement details showed better strength and ductility compared to the diagonal confinement. From the results of FB33 specimen, the maximum plastic rotation prior to the strength degradation was greater than 4%, which is much larger than the backbone curve of the coupling beams suggested by ASCE 41-13. The energy dissipation of FB33 specimen was much less than the diagonally reinforced coupling beams due to large pinching effect.

Chapter 3. Analysis Model

3.1 Synopsis of analysis model

This study aims to evaluate the seismic performance of a high-rise residential building which is planned in Seoul. The synopsis of the building is summarized in **Table 3-1**. The typical plan of the building and identifications (IDs) of members are shown in **Figure 3-1** and **Figure 3-2**.

Table 3-1 Synopsis of ACRO Seoul Forest residential building

	Contents	Notes
Size	7-story below ground/ 49-story above ground	Height: 199.9 m
Use	Residential	
Structural system	Building Frame System (Frames resist vertical load and shear walls resist lateral load)	Outrigger wall (28F) & Post-tensioning flat plate

Figure 3-1 Typical plan

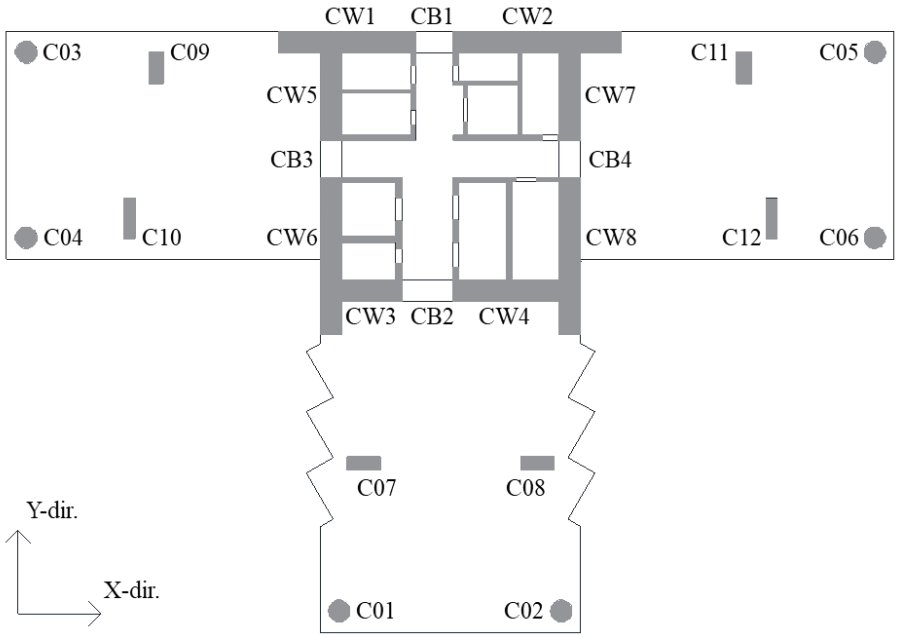

Figure 3-2 IDs of members

The height of the studied residential building is 199.9 m, which makes the structural design of the building to be governed by wind loads. Because the design of most of the members is governed by wind loads, the purpose of this study aims to evaluate the performance of the system and individual members under seismic loads based on nonlinear static and dynamic analysis using ETABS 2016. Nonlinear elements are applied only for the members that are expected to yield, and linear elements are used for other members. The expected yield range of the building is shown in **Table 3-2**. Fiber models are used to describe the inelastic behavior of walls and columns. Concentrated plastic hinges at the end of beams are employed for coupling beams.

Table 3-2 Expected yield range

	Wall	Column	Coupling beam
Expected yield range	B7~6F, 27~30F	All	All
Nonlinear model	Fiber model	Fiber model	Concentrated plastic hinge

3.2 Material model

This chapter deals with the material models. Generally, only the elastic modulus of materials is required for linear analysis. However, to use the fiber models for modeling the inelastic behavior of walls and columns in the nonlinear time history analysis, the backbone curve and hysteretic behavior of the materials should be defined.

3.2.1 Expected strength

In the nonlinear analysis, the expected strength of materials which is closer to the real strength is used rather than nominal strength. The yield of desired members can be induced as intended by performing the more accurate prediction of strength. The expected strength of materials in **Table 3-4** and **Table 3-5** are determined by the expected strength factor in **Table 3-3** suggested by the Guidelines for Performance-Based Seismic Design of Residential Buildings (2015). The elastic moduli of concrete are determined by the following equations from KCI 2012.

$$E = 8{,}500\sqrt[3]{f_{cu}} \tag{3-1}$$

where

$$f_{cu} = f_{ck} + \Delta f \tag{3-2}$$

where f_{ck} is the specified compressive strength of concrete; If f_{ck} is less than 40 MPa, Δf is 4 MPa, and if f_{ck} exceeds 60 MPa, Δf is 6 MPa. Values between 40 MPa and 60 MPa should be determined by linear interpolation.

Table 3-3 Expected strength factor

Material	Nominal strength (f_{ck} or f_y)	Expected strength factor
Concrete compressive strength	$f_{ck} \leq 21$ MPa	1.2
	21 MPa < $f_{ck} \leq 40$ MPa	1.1
	$f_{ck} > 40$ MPa	1.0
Yield and tensile strength of reinforcement	$f_y < 300$ MPa	1.25
	300 MPa $\leq f_y <$ 400 MPa	1.2
	400 MPa $\leq f_y <$ 500 MPa	1.1
	500 MPa $\leq f_y <$ 600 MPa	1.05
	$f_y \geq 600$ MPa	1.0

Table 3-4 Expected strength of concrete

Floor	Wall/Column/Beam				PT slab			
	f_{ck} (MPa)	E_c (MPa)	Expected f_{ck} (MPa)	Expected E_c (MPa)	f_{ck} (MPa)	E_c (MPa)	Expected f_{ck} (MPa)	Expected E_c (MPa)
30F~	30	27,537	33	28,324	30	27,537	33	28,324
19~29F	40	30,008	44	30,977	30	27,537	33	28,324
11~18F	49	32,108	49	32,108	35	28,825	38.5	29,663
B7~10F	59	34,159	59	34,159	45	31,210	45	31,210

Table 3-5 Expected strength of reinforcement and structural steel

Material	Yield strength (MPa)	Tensile strength (MPa)	Expected yield strength (MPa)	Expected tensile strength (MPa)	Elastic modulus (MPa)	Notes
SD400	400	560	440	616	200,000	SRC column rebars
SD500	500	620	525	651		Less than D13
SD600	600	710	600	710		Larger than D16
SHN490	325	490	390	588		SRC column steel
SM570	430 (40 < $t \leq$ 75 mm)	570	473	627		

3.2.2 Concrete model

In the nonlinear analysis using fiber elements, stress-strain curves of material are required because stiffness of members is determined by the stress-strain curves of fiber elements. Guidelines for Performance-Based Seismic Design of Residential Buildings (2015) suggests that the strain of unconfined concrete at the maximum stress shall be 0.002, and the strain at the failure shall be 0.003 with 10% of the maximum stress as residual stress.

In this study, simplified concrete stress-strain curves are used. The initial elastic modulus of concrete is assumed to remain until 85% of the maximum expected stress. And the stress of unconfined concrete is assumed to be the maximum at a strain of 0.002, and 10% of the maximum stress at strain of 0.003. The tensile stress of concrete is ignored. The comparisons of simplified stress-strain curves of concrete model and Popovics's concrete model (Popovics, 1973), which is the basis of Mander's unconfined concrete model (Mander et al, 1988), are shown in **Figure 3-3**.

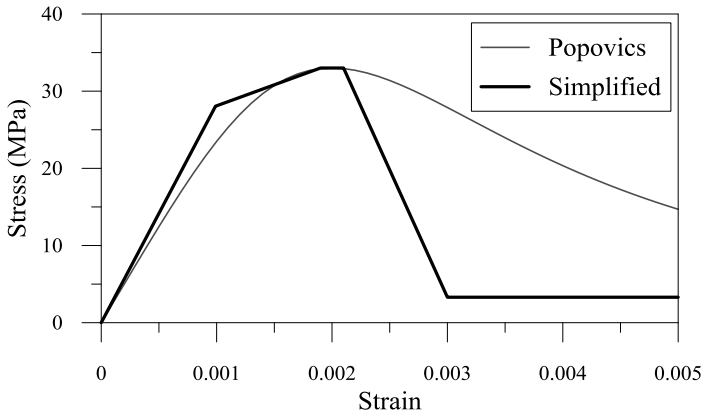

(a) C30

Figure 3-3 Stress-strain curves of concrete (continued)

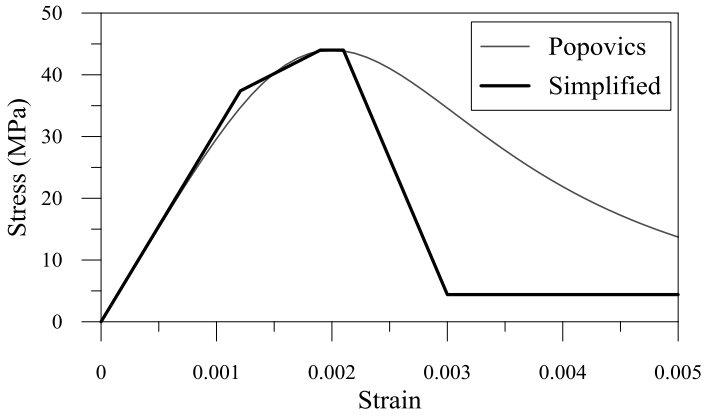

(b) C40

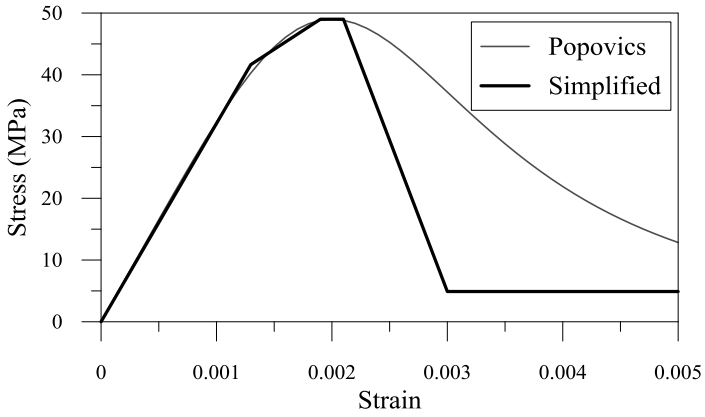

(c) C49

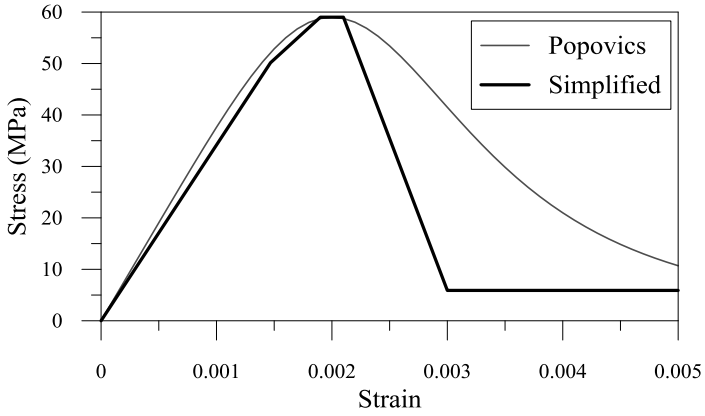

(d) C59

Figure 3-3 Stress-strain curves of concrete

The concrete hysteresis model in ETABS 2016 is used for concrete fiber elements. This model reflects stiffness degradation, and the unloading slope at the maximum force is half of that of initial loading. There is one parameter in the concrete hysteresis model, that is energy degradation factor. This factor is related to the delay of strength reduction due to cracks after the elastic range. The value of this factor is from 0 to 1.0. The larger the factor, the energy dissipation area becomes larger. As shown in **Figure 3-4**, an energy degradation factor of 0.7 is used for the concrete hysteresis model in this study.

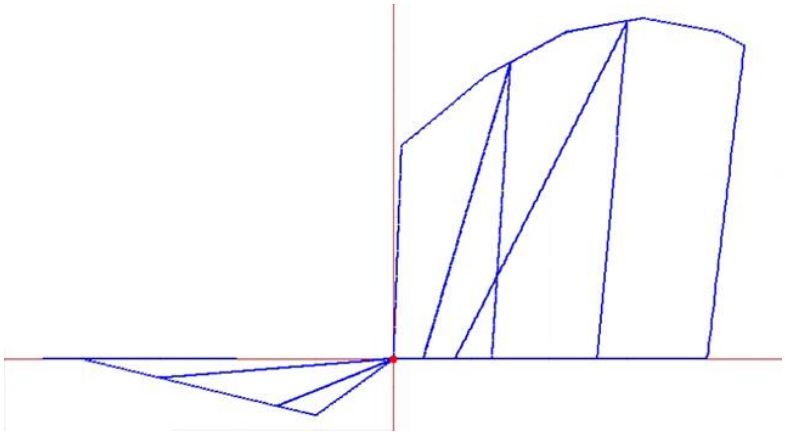

Figure 3-4 Concrete hysteresis model with energy degradation factor of 0.7 (Computers and Structures Inc., 2016)

3.2.3 Reinforcement model

SD400, SD500, and SD600 rebars are high-strength reinforcement, and generally the ductility of a high-strength rebar is less than that of a normal-strength rebar. From the experiment results of Lee et al. (2010), the maximum strength of a high-strength rebar is assumed to occur at strain of 0.05, and the strength is conservatively assumed to be 0 at a strain of 0.06. The stress-strain curve for compression and tension is assumed to be the same. The buckling of rebars is not considered. The stress-strain curves for SD400, SD500, and SD600 are shown in **Figure 3-5**.

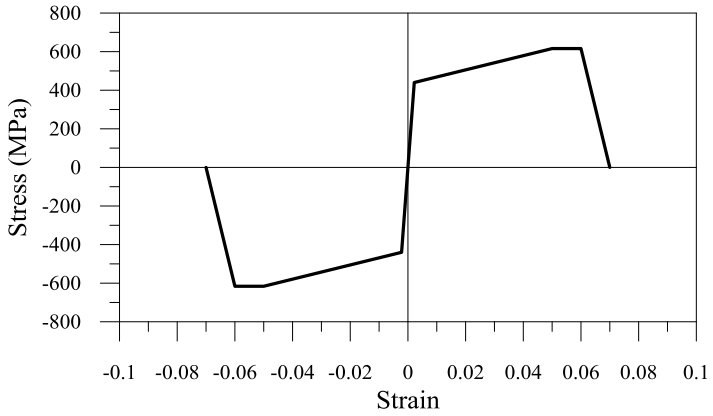

(a) SD400

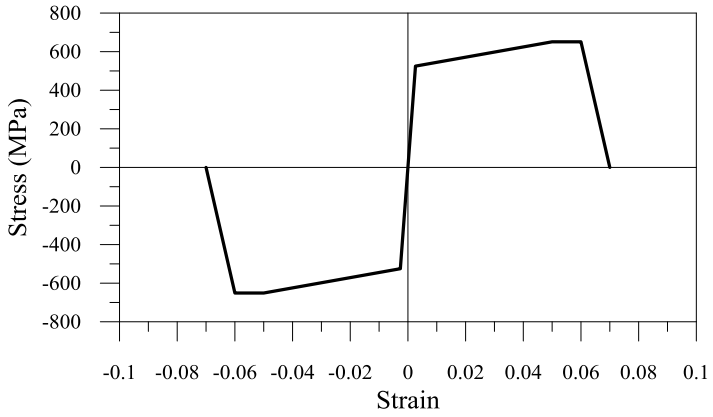

(b) SD500

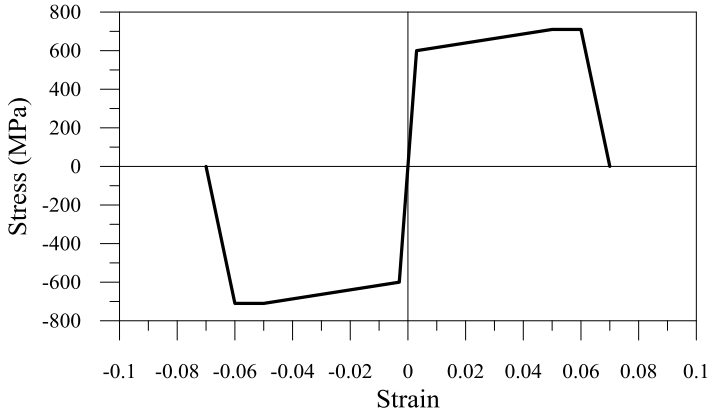

(C) SD600

Figure 3-5 Stress-strain curves of reinforcement

The kinematic hysteresis model of ETABS 2016 shown in **Figure 3-6** is used for modeling the hysteretic behavior of rebars. This model is appropriate for ductile metals, and has a large energy dissipation area. It can describe the hardening of metal along the backbone curve. The unloading stiffness is the same as initial stiffness and does not decrease according to the hysteretic behavior. The yielding due to reverse loading occurs at the same length as the previous loaded line, and the curve meets backbone curve with the same hardening stiffness of previous loading. The kinematic hysteresis model may overestimate the energy dissipation capacity of rebars, because it cannot describe the stiffness and strength degradation according to plastic deformation and repeating cyclic loads. Although it has limitations, it can capture the hysteretic behavior of reinforcement at the relatively small plastic deformations. Because the vertical members of this building model are expected to undergo small plastic deformations, the use of kinematic model can be reasonable.

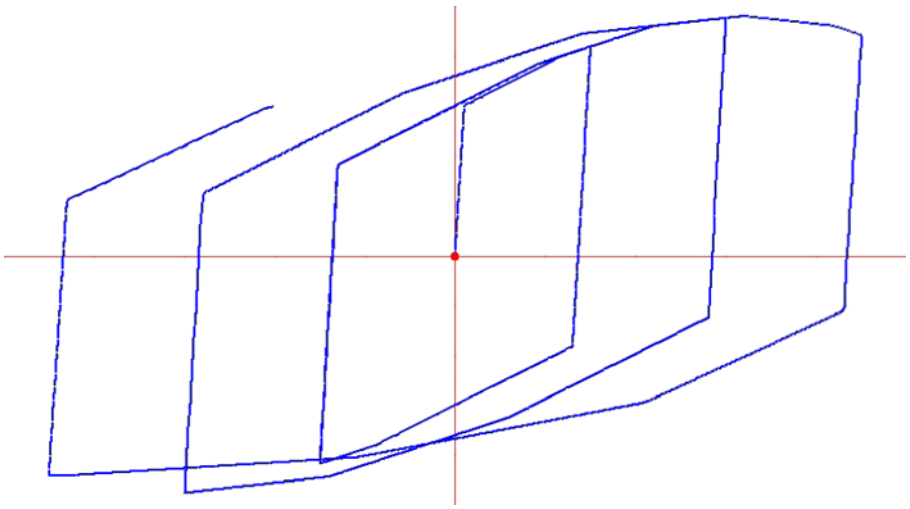

Figure 3-6 Kinematic hysteresis model (Computers and Structures Inc., 2016)

3.2.4 Structural steel model

The modeling of structural steel materials for Steel-RC (SRC) columns with the yield strength exceeding 400 MPa is the same as that of high-strength rebars. However, the ordinary strength steel with the yield strength less than 400 MPa is assumed to fail at a strain of 0.11 after strength degradation at a strain of 0.1 due to the large ductility of normal strength steel. The stress-strain curve of steel is shown in **Figure 3-7**. The same hysteresis model of rebars is used for structural steel.

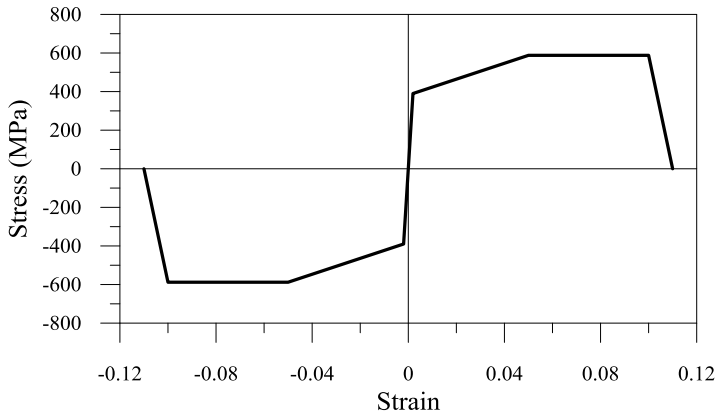

(a) SHN490

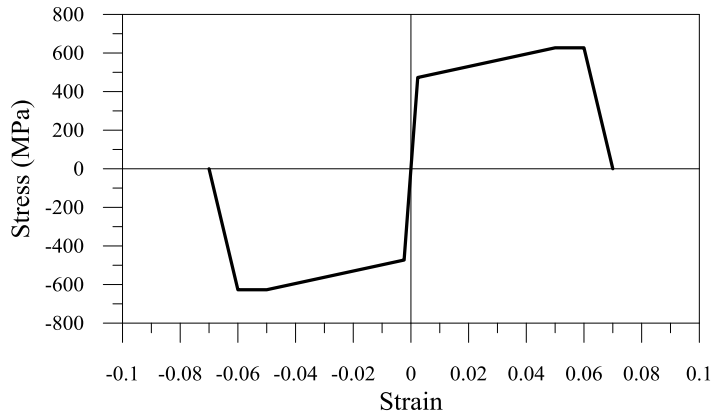

(b) SM570

Figure 3-7 Stress-strain curves of structural steel

3.3 Modeling of slabs

The modeling of slabs is not included in typical current design practice, and only rigid diaphragm is used instead, which is a conservative design method commonly used in design practice. The neglect of the out-of-plane bending stiffness of slabs leads to an underestimation of lateral stiffness of the building. It also leads to an overestimation of the period of the building and underestimation of associated seismic force. Especially, for post-tensioned slabs with a relatively large stiffness, the slab stiffness may need to be considered.

In this analysis model, elastic shell elements are used for the modeling of slabs, because there are no nonlinear models for inelastic behaviors of slabs in ETABS 2016. Instead, the out-of-plane stiffness is reduced by considering the cracking and inelastic behavior of the slabs. Kang and Wallace (2005) suggested the effective stiffness factor for cracking, β-values, of 1/3 and 2/3 for RC and post-tensioned (PT) slab-column frame system, respectively. It means that a PT slab has twice of the effective stiffness of a RC slab. Because the effective stiffness of $0.1EI_g$ is commonly used for a RC slab in Korean design practice, it is assumed that PT slabs have the effective stiffness of $0.2EI_g$ in this study.

3.4 Modeling of outrigger walls

As shown in **Figure 3-8**, 800 mm thick outrigger walls are used at the 28th floor. These outrigger walls act as beams and transfer lateral loads to the perimeter columns. Unlike general shear walls, it is difficult to apply the nonlinear model using fiber elements in the vertical direction for the outrigger walls. Thus, outrigger walls are assumed to be elastic, but the effective stiffness is reduced by considering the inelastic behaviors. The effective stiffness of outrigger walls is applied by reducing the modulus of elasticity of concrete as 35%. The out-of-plane stiffness of outrigger walls is reduced to $0.25EI_g$.

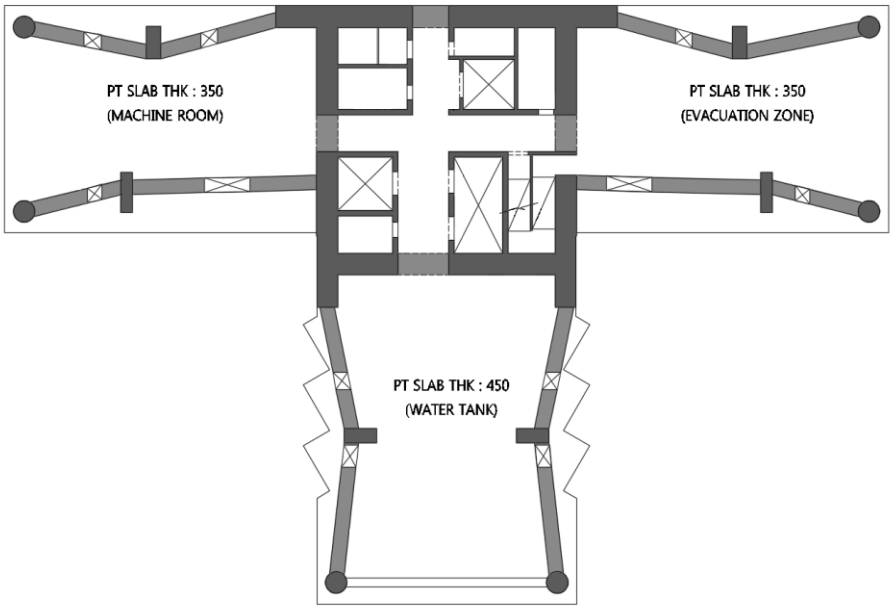

Figure 3-8 Structural plan of 28th floor

3.5 Modeling of vertical members

As shown in **Figure 3-9**, there are three types of inelastic models; 1) continuum model, 2) distributed inelasticity model (fiber model), and 3) concentrated hinge model. The continuum model is a physical model which describes the inelastic behaviors based on the physics of materials. But it is not appropriate for modeling of a whole structure due to the large amount of computational efforts. The distributed inelasticity model, called as fiber model, is used for modeling of inelastic behaviors of vertical members. The effective stiffness is calculated based on the stress-strain relationship of materials in the fiber elements.

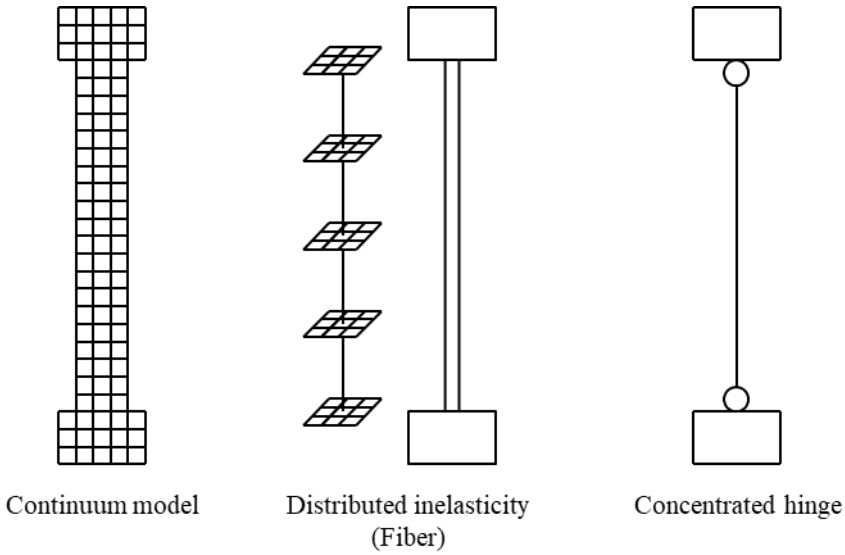

Figure 3-9 Types of inelastic models

3.5.1 Fiber model for columns

The P-M2-M3 fiber model in ETABS 2016 is used to describe the nonlinear behavior of columns, because columns are assumed to be controlled by flexure rather than shear. The P-M2-M3 fiber model can reflect the P-M

interaction of two perpendicular axes. A column is divided into 5 elements along the longitudinal direction to capture flexural failure at each end of the column, and the fiber elements are applied to the center of each of the divided elements. Each fiber length is set to be 20% of the column length.

The fiber model of circular shape columns and square shape SRC columns are shown in **Figure 3-10**. The hatched areas in SRC columns are fibers of steel. The circular shape column is simplified as a dodecagon. In case of SRC column, the fiber areas of wide flange beam and concrete are set not to overlap. The fibers of rebars are set at each position as many as the actual number of rebar, and the areas overlapping with concrete fibers are ignored.

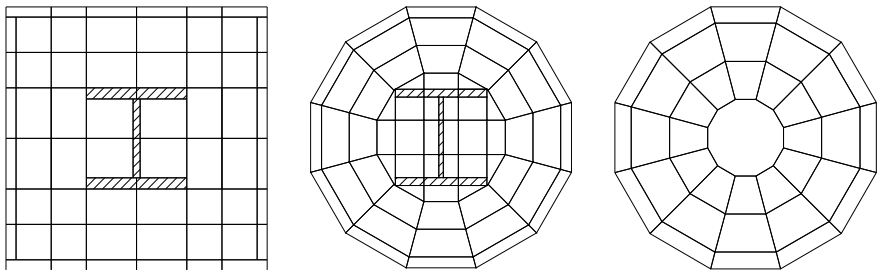

(a) Square shape SRC (b) Circular shape SRC (c) Circular shape RC

Figure 3-10 Fiber models of square and circular shape columns

The fiber models of rectangular shape columns are shown in **Figure 3-11**. The principle of fiber modeling of rectangular shape columns is the same as that of circular columns.

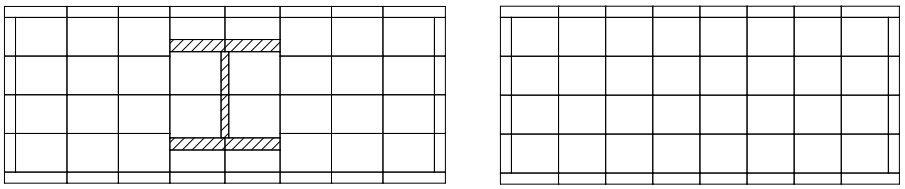

(a) Rectangular shape SRC (b) Rectangular shape RC

Figure 3-11 Fiber models of rectangular shape columns

3.5.2 Fiber model for walls

The P-M3 fiber model in ETABS 2016 is used for the inelastic behavior modeling of core walls. The P-M3 fiber model can model the P-M interaction with respect to one axis, the in-plane direction of shell elements. Because the P-M3 fiber model cannot consider the out-of-plane nonlinear behavior of shell elements, which means that the out-of-plane behavior is linear, the effective stiffness of $0.25\,EI_g$ is used for the out-of-plane bending stiffness of core walls.

From the linear analysis, the fiber model is applied to the core walls of B7th to 6th and 27th to 30th floors where the nonlinear behaviors are expected. The linear shell element is used for core walls of the other floors, and the effective stiffnesses of 70% and 25% of gross section are taken for membrane and out-of-plane stiffnesses, respectively.

3.6 Modeling of coupling beams

Lequesne et al. (2016) studied the cyclic behavior of coupled shear walls with fiber reinforced concrete. From the paper, the chord rotation of coupling beams is calculated by following equation.

$$\theta_{chord,i} = \frac{(\Delta_{w,i} + \theta_{w,i} L_w) - (\Delta_{e,i} - \theta_{e,i} L_w)}{L_b} + \frac{(\theta_{w,i} + \theta_{e,i})}{2} \quad (3\text{-}3)$$

where $\Delta_{e,i}$ and $\Delta_{w,i}$ are the relative vertical deformations of the east and west walls at the level *i*, respectively; $\theta_{e,i}$ and $\theta_{w,i}$ are the wall rotations of the east and west walls at the level *i*, respectively; L_w is the horizontal length of the east and west wall; and L_b is the clear span of the coupling beam.

From the above equation, neglecting the vertical deformations of each shear wall, the equation can be simplified as the following:

$$\theta_{chord,i} = (\theta_{w,i} + \theta_{e,i})(\frac{L_w}{L_b} + \frac{1}{2}) \quad (3\text{-}4)$$

From the above equation, the chord rotation of a coupling beam is affected by the rotation of shear walls and the ratio between the length of a wall and a coupling beam. Generally, the horizontal length of walls is larger than the clear span of a coupling beam. Coupling beams experience larger deformation than shear walls under lateral loads, which causes yielding of coupling beams before the yielding of shear walls. Therefore, the accurate models for inelastic behavior of coupling beams are required, and this study focuses on the modeling of coupling beams.

The studied building has 1,200 mm thick core walls. These shear walls resist lateral loads with very large stiffness compared to the coupling beams. The horizontal lengths of core walls are also larger than the span of coupling

beams, and the coupling beams are expected to experience large deformation. So the nonlinear models of coupling beams are applied to the whole stories. The coupling beams have relatively large span-to-depth ratio of 3.3 and 4.7, and they are expected to be controlled by flexure. Thus, concentrated moment hinges at the each end of a coupling beam are used to describe its nonlinear behavior. The moment hinges have infinite stiffness until the applied moment reaches to the yield moment. The behavior of coupling beams is governed by the nonlinear behavior of moment hinges after the yield moment.

3.6.1 Effective stiffness of coupling beam

ACI 318-14 suggests the effective stiffness of beams as $0.35E I_g$, and ASCE 41-13 suggests as $0.3E I_g$. These values may not be appropriate for coupling beams, because there are differences between the behavior of coupling beams and that of ordinary beams. From the experiment results of Naish et al. (2013), PEER/ATC 72-1 suggests the effective stiffness of coupling beams as $0.15E I_g$, which will be verified in **Section 3.6.4**.

3.6.2 Backbone curve of coupling beam

ASCE 41-13 suggests the backbone curve of RC coupling beams. The strength of the backbone curves of RC coupling beams with conventional longitudinal reinforcement and transverse reinforcement in accordance with ASCE 41-13 begins to decrease after the plastic chord rotation of 2 to 2.5%. The residual strengths are 0.5 to 0.75 of the yield strength, and the strengths finally drop to zero at the plastic chord rotation of 3.5 to 4.0%. ASCE 41-13 also permits to use a backbone curve from experimental results or other reliable evidence.

From the experimental results from Xiao et al. (1999) and Naish et al. (2013), the backbone curves from ASCE 41-13 seem to be conservative. Such differences of the backbone curve between the experimental results and ASCE 41-13 seem to be due to the span-to-depth ratio. Although there are many

factors affecting the ductility of coupling beams, such as the arrangement of longitudinal rebars, steel ratios of longitudinal and transverse rebars, strength of materials, and embedment of rebars, there is a more pronounced tendency between the ductility and span-to-depth ratio of coupling beams designed by general codes. **Figure 3-12** shows the relationship between the maximum plastic chord rotation and span-to-depth ratio of coupling beams with conventional longitudinal reinforcement and conforming transverse reinforcement in various experimental studies performed by Xiao et al. (1999), Lim et al. (2016a and 2016b), Naish et al.(2013), and Galano and Vignoli (2000). Here, the maximum plastic chord rotations are determined from the plastic rotation before the significant strength degradation, and the significant strength degradation indicates that the strength becomes less than 90% of the maximum strength.

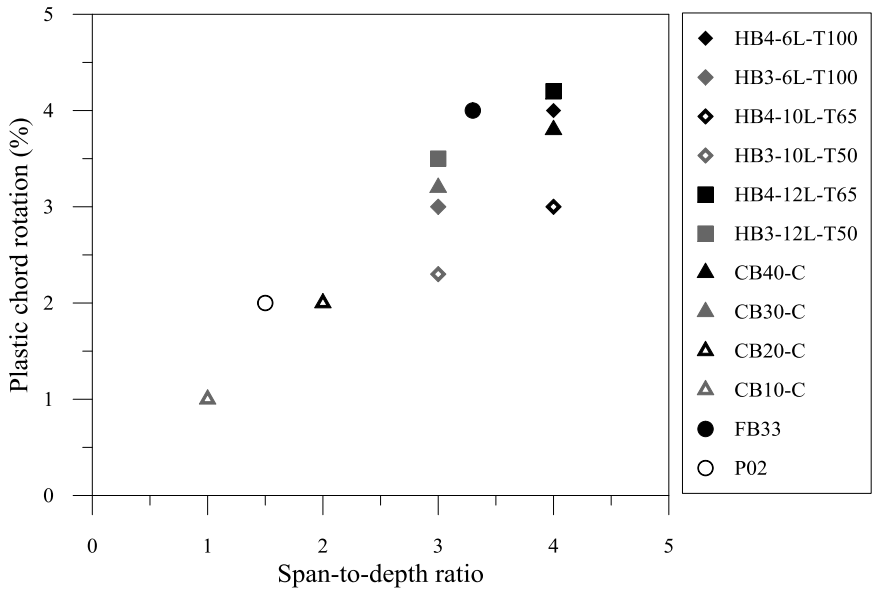

Figure 3-12 Relationship between span-to-depth ratio and plastic chord rotation

The experimental results of coupling beams from the literatures in **Figure 3-12** also show that the strength drops quickly after the onset of the strength

degradation without much residual strength. From the experimental results, the application of the backbone curves from ASCE 41-13 is turned out to be improper for the coupling beams with span-to-depth ratios of 3.3 to 4.7. Thus, the following backbone curve is used. The elasto-plastic behavior after the yielding is used. The maximum plastic chord rotation before strength degradation is assumed to be 3%, and the coupling beam is assumed to fail at a plastic rotation of 4.5%. This is based on the results of HB4-10L-T65 specimen tested by Xiao et al. (1999) which showed the lowest maximum plastic rotation among the specimens with a span-to-depth ratio of 4. The yield moments of coupling beams are automatically calculated by ETABS 2016 based on the expected strength of materials and section of the coupling beam.

3.6.3 Hysteretic behavior of coupling beam

Accurate representation of the hysteresis curve of the coupling beams expected to yield is very important in nonlinear dynamic analysis, because the energy dissipation during nonlinear dynamic analysis is governed by hysteretic behavior of a series of members rather than its viscous damping. However, there are few guidelines or codes which deal with the modeling of hysteresis curves, and generally experimental data related to members are used.

The pivot hysteresis curve model in ETABS 2016 which is suggested by Dowell et al. (1998) is employed. This model is based on experimental observations that reloading of RC member leads to a specific point called as the pivot point. The pivot hysteresis model shown in **Figure 3-13** is determined by following three parameters, α, β, and η.

α: It locates the pivot point for unloading to zero from the backbone curve after the plastic deformation.

β: It locates the pivot point on the initial loading line when reloading occurs.

Reloading occurs toward the point on the elastic line at the forces value of β times the yield force.

η : It is a factor for the degradation of the reloading stiffness after yielding.

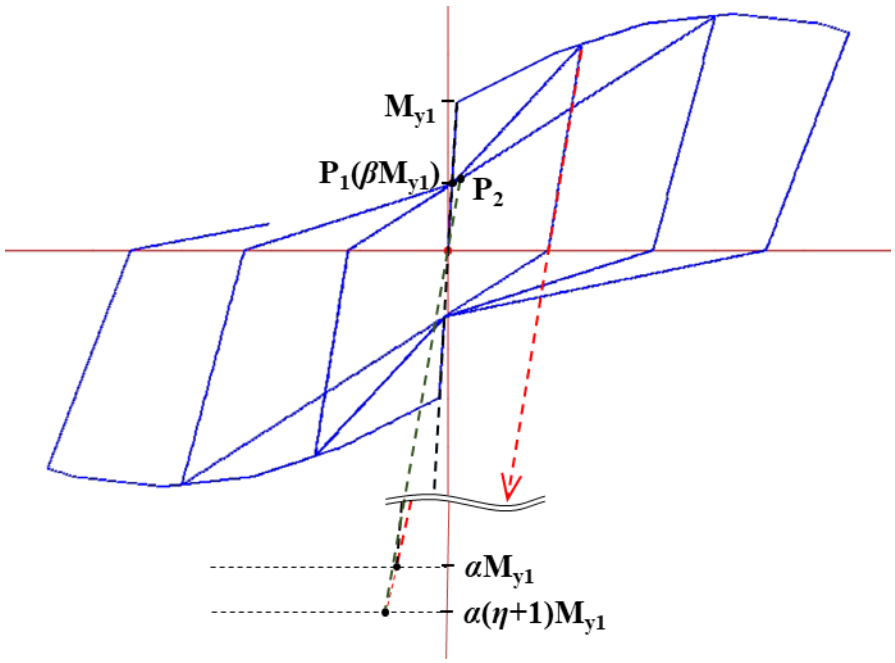

Figure 3-13 Pivot hinge model (Computers and Structures Inc., 2016)

The advantage of this model is that it can describe the hysteresis curves of concrete members with the experimental observations, and captures the actual behavior, like the pinching effect.

To use the pivot hysteresis model, these parameters for coupling beams should be properly determined. In this study, the HB4-10L-T65 specimen of Xiao et al. (1999) is used to determine the hysteresis curve of the RC coupling beam, because the span-to-depth ratio, arrangement of rebars, and steel ratio are similar to the analysis model. From the experiment results of Xiao et al. (1999), the degradation of unloading stiffness is not significant, and the energy dissipation area is mainly characterized by pinching effect. And from

the results of Xiao et al. (1999), it seems that the location of pivot point on the initial elastic line is affected by the longitudinal reinforcement ratio and span-to-depth ratio. **Figure 3-14** shows the relation between the longitudinal reinforcement ratio and β of the pivot hysteresis model. It seems that the β divided by the square of span-to-depth-ratio increases proportionally to the longitudinal steel ratio. Therefore the parameter for the pivot point on the initial loading line, β, can be determined by the following equation.

$$\beta = a^2(0.0047\rho + 0.0036) \tag{3-5}$$

where

a: span-to-depth ratio of RC coupling beam

ρ: longitudinal reinforcement ratio

Because the longitudinal reinforcement ratios of coupling beams in the analysis model are varied, β is determined by **Eq. (3-5)**. In order to define the hysteretic behavior of coupling beams using the pivot model, α and η also should be defined. The degradation ratios of unloading stiffness and reloading stiffness after the pivot point are similar regardless of the specimens. So α and η for general RC coupling beams is determined as in **Section 3.6.4**.

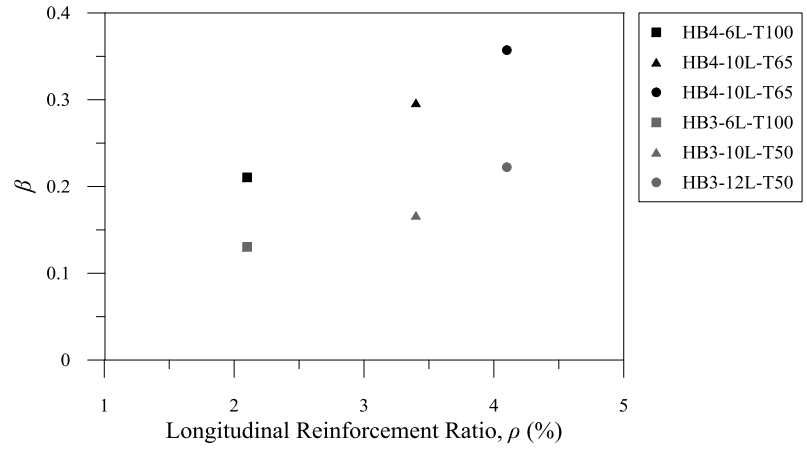

(a) Relationship of β and ρ

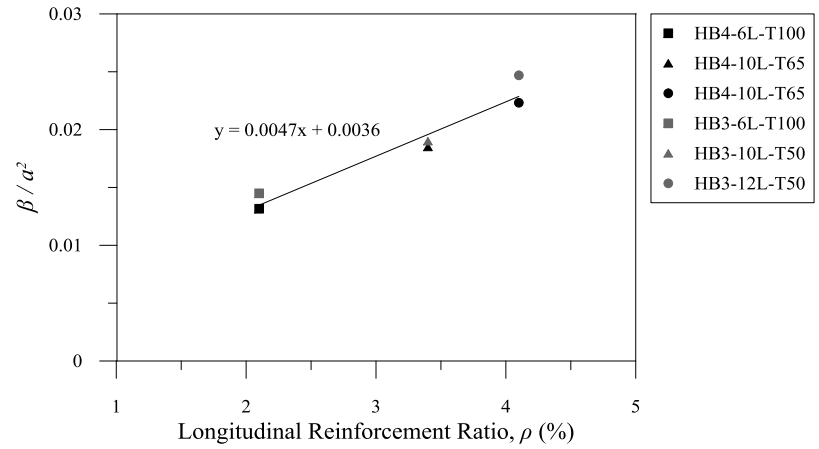

(b) Relationship of β/a^2 and ρ

Figure 3-14 Relationship of β, a, and ρ

3.6.4 Verification

The modeling parameters of coupling beams are verified using the experimental results of Xiao et al. (1999). In the verification model, the strength and elastic modulus of concrete and reinforcement, yield moment, and backbone curve are extracted from the test results. The values of α and η

of the pivot hysteresis model are determined from the specimen of Xiao et al. (1999), and these values are used for the analysis model. The results are compared in **Figure 3-15**, and showing that the concentrated plastic hinge with the pivot hysteresis model can accurately describe the nonlinear behavior of the RC coupling beam. The values of α and η of 3 and 0.1, respectively, seem to be applicable for a general RC coupling beam. Furthermore, the effective stiffness of $0.15EI_g$ suggested by PEER/ATC 72-1 seems reasonable.

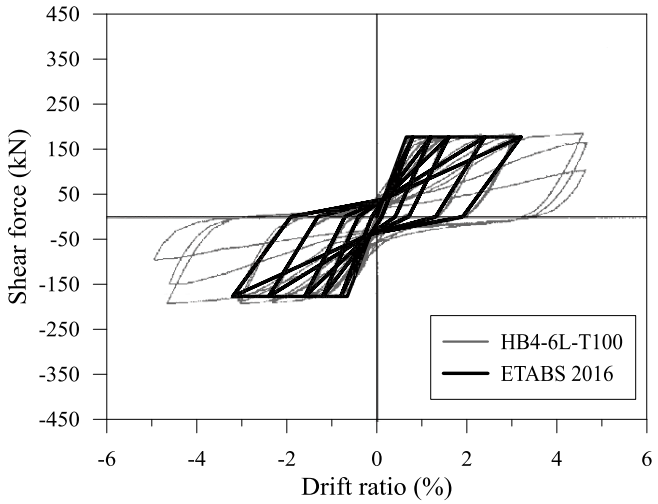

(a) HB4-6L-T100 (α = 3, β = 0.22, and η = 0.1)

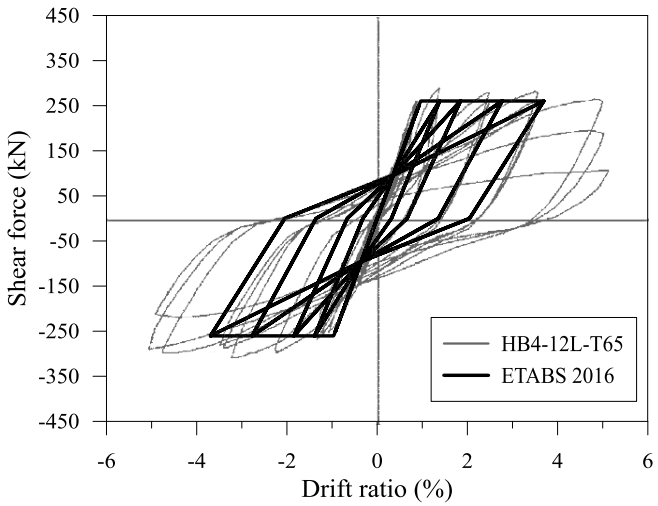

(b) HB4-6L-T100 (α = 3, β = 0.36, and η = 0.1)

Figure 3-15 Hysteretic modeling of coupling beams (continued)

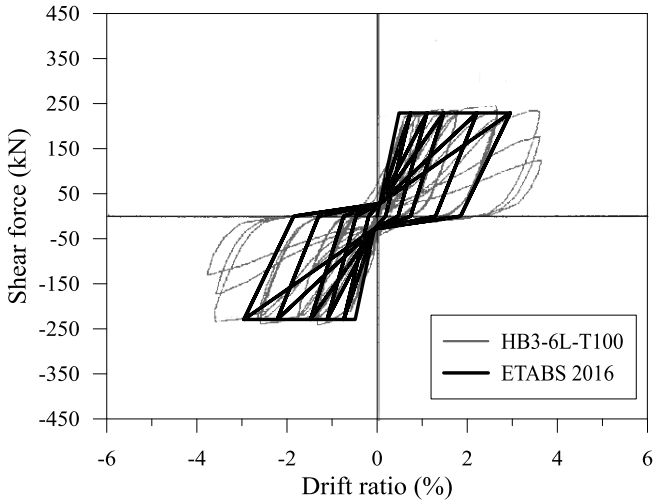

(c) HB3-6L-T100 (α = 3, β = 0.12, and η = 0.1)

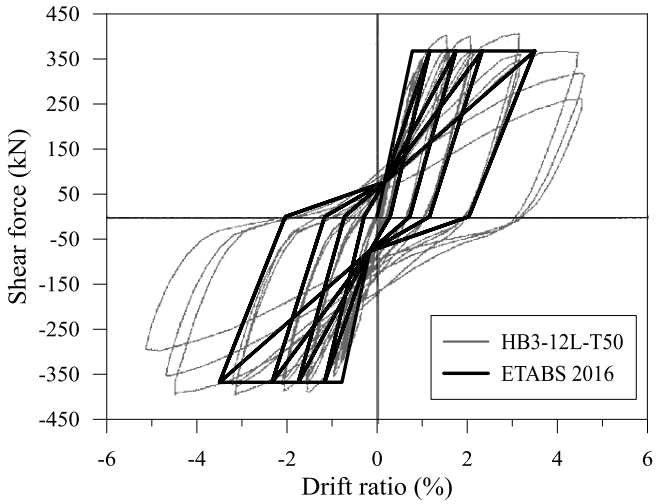

(c) HB3-12L-T50 (α = 3, β = 0.21, and η = 0.1)

Figure 3-15 Hysteretic modeling of coupling beams

3.7 Modeling of underground structure

In the seismic design, the modeling of underground structures and soil-structure interaction is necessary. However, it is difficult to model the nonlinear behavior of surrounding soils in Korea due to the lack of detailed relevant information. So in actual design practice, the modeling of underground structure is often excluded, or the modeling of underground structures is included without consideration of the effect of surrounding soils. Such modeling methods lead to an underestimation of story shear force at the ground level or an overestimation at the base. According to the study by Tocci and Levi (2012), tall buildings generally have a huge underground structure due to parking lots, and floor slabs of the underground structure have very large in-plane stiffness. These diaphragms act as lateral supports under lateral forces, which is called as a backstay effect. Therefore, the existence of a certain underground structure model and boundary condition significantly affect the distribution of story shear forces at the basement.

The Guidelines for Performance-Based Seismic Design of Tall Buildings (TBI 2017) suggests several basement modeling methods as shown in **Figure 3-16**. According to TBI 2017, the modeling of actual soil-structure-interaction is very difficult. Therefore, the fixed-base model without considering the soil-structure-interaction (Figure 3-16 (b)) is recommended for a design practice. This model neglects the lateral stiffness contribution of the surrounding soils. The modeling of the whole basement including the underground perimeter walls is required in this model.

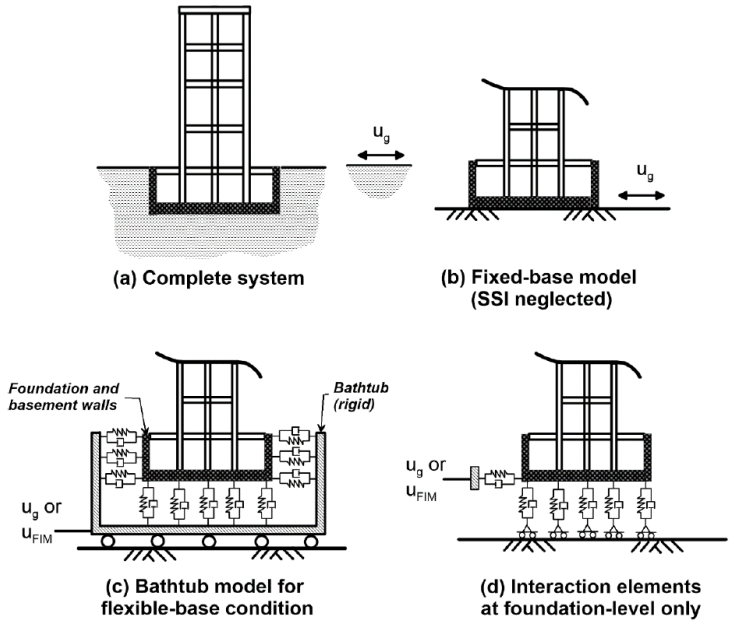

Figure 3-16 Schematic illustration of basement models (TBI 2017)

In this study, it is assumed that underground structures and surrounding soils translate horizontally together, because underground perimeter walls are sufficiently stiff and the condition of surrounding soil is favorable. Additionally, the building also has huge underground parking lots with relatively large in-plane stiffness slabs. So as shown in **Figure 3-17** the underground structure model is included to consider only the vertical deformation, with roller boundary conditions on the sides and fixed conditions at the bottom of the basement. The earthquake loads are applied to the whole basement.

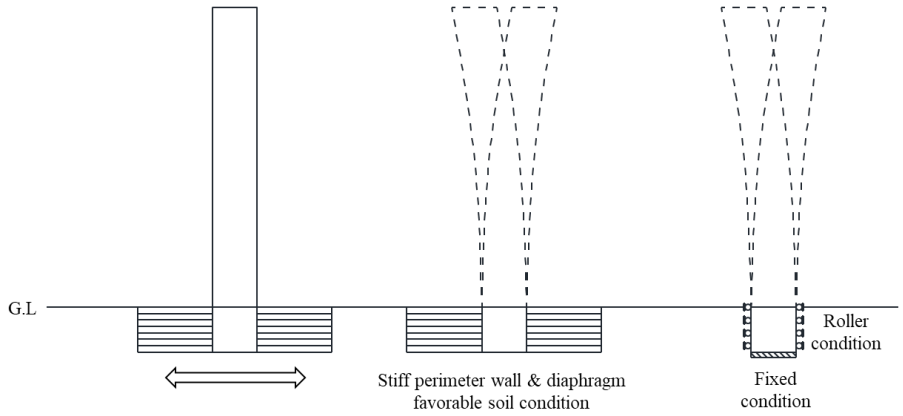

Figure 3-17 Modeling of underground structure

In order to examine the influence of underground modeling methods, the laterally supported model is compared with the basement model suggested by TBI 2017. As suggested by TBI 2017, the basement structure surrounding the building is included without considering the soil-structure-interaction. Because the surrounding underground parking lot is too large to be entirely included, the surrounding parking lot is partially included as shown in **Figure 3-18**. To consider the actual in-plane deformation of the slabs of the underground parking lot, semi-rigid diaphragm is used for the slabs at the basement. The comparison model is shown in **Figure 3-19**. The comparison results are discussed in **Section 6.5**.

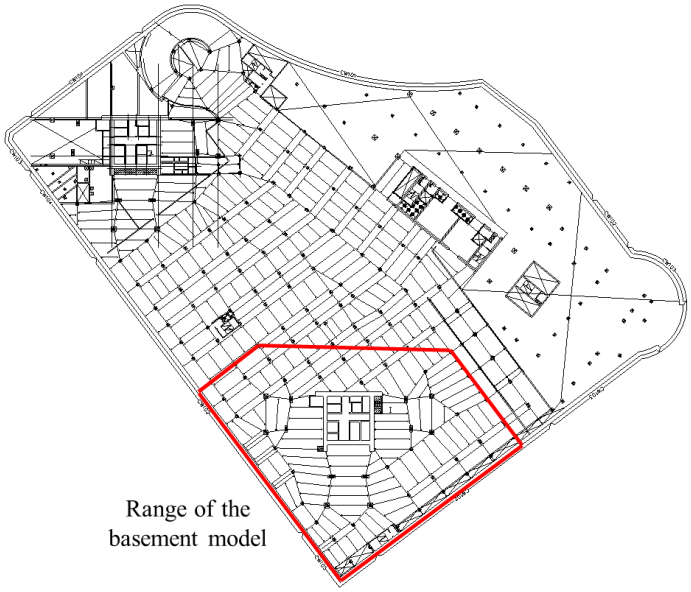

Figure 3-18 Basement structural plan

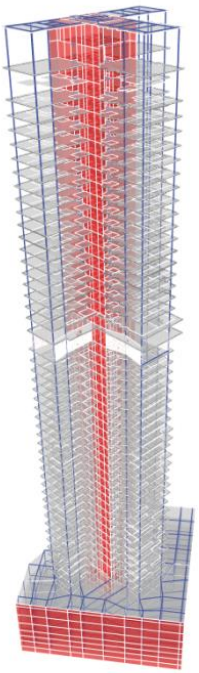

Figure 3-19 Basement model suggested by TBI 2017

3.8 Modal analysis results

To define the Rayleigh damping, modal analysis should be performed prior to nonlinear time history analysis. The modal analysis results of ETABS nonlinear model are compared with those of the initial linear models using MIDAS Gen in **Table 3-6**. There are differences between the results of the two analysis models. The MIDAS Gen model has the core walls with no out-of-plane stiffness and the larger effective stiffness of the coupling beams. On the other hand, the ETABS nonlinear model has the core walls with $0.25EI_g$ out-of-plane stiffness, as well as consideration of flange contributions of T- or C-shaped walls, and the slabs with $0.2EI_g$. The effective stiffness of the coupling beams is $0.15EI_g$.

Table 3-6 Modal analysis results comparison

Mode	Period (sec)	
	MIDAS Gen linear model (Effective stiffness: wall_in-plane 70%; wall_out-of-plane 0%; beam 35%; outrigger wall 35%; PT slab 0%)	ETABS 2016 nonlinear model (Effective stiffness: wall_in-plane 70%; wall_out-of-plane 25%; beam 15%; outrigger wall 35%; PT slab 20%)
1st	7.96	7.54
2nd	6.83	6.12
3rd	5.23	5.21
4th	2.35	2.39
5th	1.80	1.81
6th	1.66	1.71
7th	1.15	1.13
8th	0.80	0.79
9th	0.78	0.76
10th	0.70	0.69

3.9 Damping

Responses of a nonlinear dynamic analysis are sensitive to damping, and the selection of damping ratio is important. Generally 5% viscous damping is used for linear analysis including the energy dissipation due to inelastic hysteretic behavior. Because inelastic behavior produces hysteretic damping in a nonlinear dynamic analysis, the viscous damping ratio should be less than that of linear analysis. ASCE 41-13 suggests that the target elastic effective viscous damping ratio shall not exceed 3% for nonlinear dynamic analysis.

According to PEER/ATC 72-1, there is a tendency that the damping ratios decrease as the height of building increases, and an equivalent viscous damping of nonlinear response history analysis is suggested as the following equations:

$$D = \alpha / 30 \quad (\text{for} \quad N < 30) \tag{3-4}$$

$$D = \alpha / N \quad (\text{for} \quad N > 30)$$

where

D: the maximum critical damping (%)

N: the number of stories

α: the coefficient for structural system ($60 \leq \alpha \leq 120$)

α = 60 for steel structures; and α = 120 for reinforced concrete structures

From the equations, the equivalent viscous damping ratio is calculated as 2.1%, and in this study the damping ratio of 2.0% is conservatively used.

Only the Rayleigh damping is available in the direct integration time history analysis of ETABS 2016. To define the Rayleigh damping, target damping ratios at two periods are needed. The target damping ratio is used as the value obtained previously. The X-direction 1st mode, which is the fundamental period of the building, and Y-direction 2nd mode, which has a shorter period

than that of X-direction 3rd mode, are used for the two periods. The damping is set as shown in **Figure 3-20**. The damping ratios of X-direction 2nd and 3rd modes and Y-direction 1st mode are less than the target damping ratio of 0.02 due to the characteristics of Rayleigh damping. The damping ratios of higher order modes increase dramatically, but the contributions of higher order modes are significantly reduced.

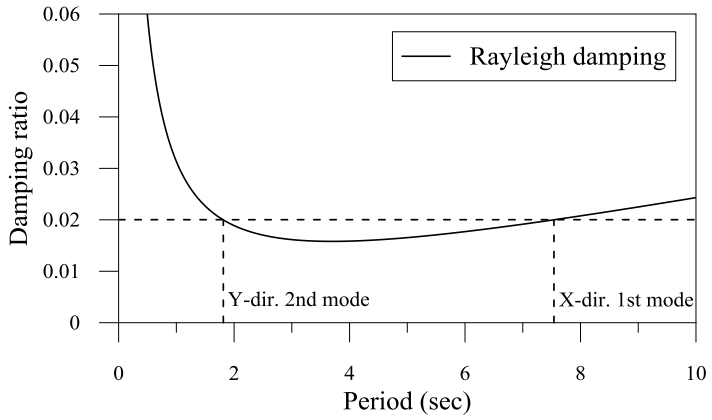

Figure 3-20 Rayleigh damping input

Chapter 4. Ground Motion Records

KBC 2016 requires using not less than three ground motion records for time history analysis. The maximum response shall be used for three ground motion records, and the average response is permitted if seven or more ground records are used. The average spectra of ground motions shall not be less than 90% of 1.3 times the target spectra for the period range from $0.2T$ to $1.5T$, where T is the fundamental period of the structure. The spectra of ground motions shall be determined by the square root of sum of squares (SRSS) combination of one horizontal component and its perpendicular component. In this study, nonlinear time history analyses are conducted for two target spectra, Design Basis Earthquake level and Maximum Considered Earthquake level. Seven ground motions for each target spectra are selected, and scaled to match the target spectra.

4.1 Design Basis Earthquake (DBE) records

4.1.1 Response spectrum of DBE

The design basis earthquake level is defined as the earthquake with 10% probability of occurrence in a 50-year-exposure period. The DBE spectrum is determined by KBC 2016. The effective peak ground acceleration of the site, S, is 0.176g. The site class was determined as S_C from the site investigation. The design earthquake spectral acceleration for short periods, S_{DS}, and the design earthquake spectral acceleration for 1-second period, S_{D1}, are determined by the following equations in KBC 2016.

$$S_{DS} = S \times 2.5 \times F_a \times \frac{2}{3} \tag{4-1}$$

$$S_{D1} = S \times F_v \times \frac{2}{3} \tag{4-2}$$

where

F_a: the short period amplification factor, F_a is 1.2 for site class S_C.

F_v: the mid period amplification factor, F_v is 1.62 for site class S_C.

The target response spectra of DBE are shown in **Figure 4-1**.

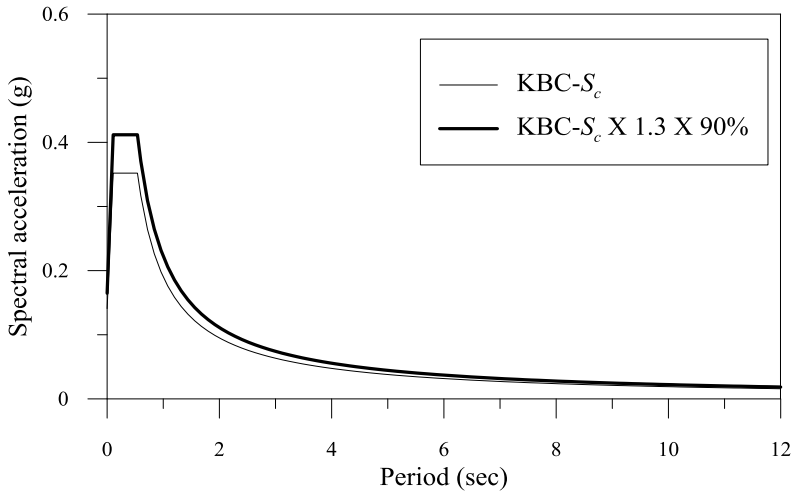

Figure 4-1 Response spectra of DBE

4.1.2 Ground motion records of DBE

Seven ground motion records shown in **Table 4-1** are selected for the ground motion records. The sampling time step of 0.05 seconds for all ground motions are used to reduce the analysis time. From the Nyquist frequency theory, if the sampling frequency is 20 Hz, the distinguishable frequency is half of the sampling frequency, 10 Hz. So in this case, the high frequency components of ground motions higher than 10 Hz cannot be recognized. However, the building has a very long fundamental period, and the high frequency components of ground motions do not affect significantly.

The ground motion records are scaled for the period range from 0.2T to 1.5T, 1.22 to 11.31 seconds, respectively. The average SRSS response spectrum of

scaled DBE ground motion is shown in **Figure 4-2**. **Figure 4-3** shows each DBE ground motion record and response spectrum of the record.

Because the ground motion records are scaled considering the local site effect and the same scaling factor is used for all the period ranges, the average of response spectra is much larger than the KBC design spectrum at the high-frequency ranges. As shown in **Figure 4-3**, the average of response spectra shows the peak at the period of near 0.2 seconds which is close to the elastic site period of 0.198 seconds.

Table 4-1 Selected ground motions

ID	EQ name	Station	Magnitude	Distance (km)
EQ1	Loma Prieta	Piedmont Jr High School Grounds	6.93	73
EQ2	Loma Prieta	SF – Pacific Heights	6.93	76
EQ3	Kocaeli	Gebze	7.51	11
EQ4	Chi-Chi	ILA015	7.62	85
EQ5	Chi-Chi	TAP067	7.62	97
EQ6	Duzce	Lamont 1060	7.14	26
EQ7	Chi-Chi	TAP075	7.62	109

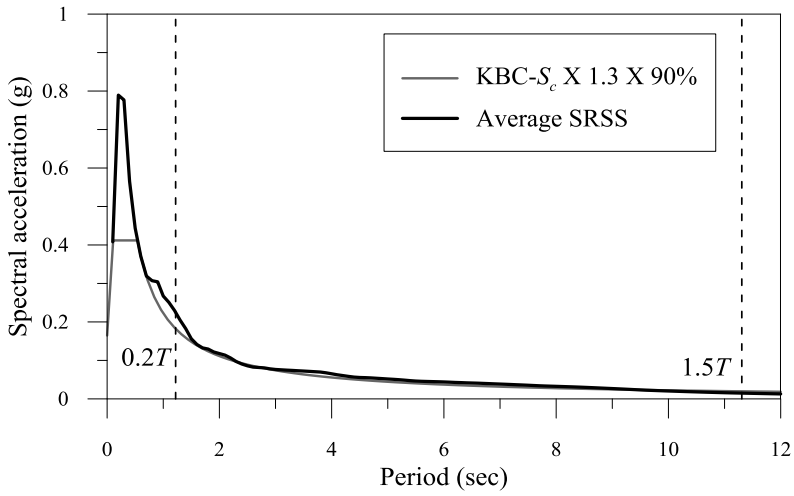

Figure 4-2 Average SRSS response spectrum of scaled DBE ground motions

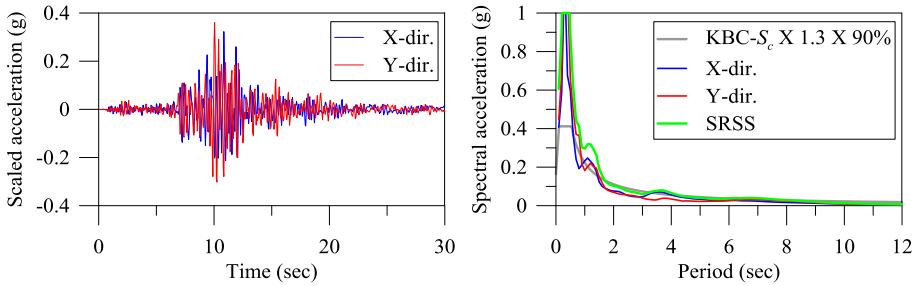

(a) DBE EQ1 Loma Prieta - Piedmont Jr High School Grounds

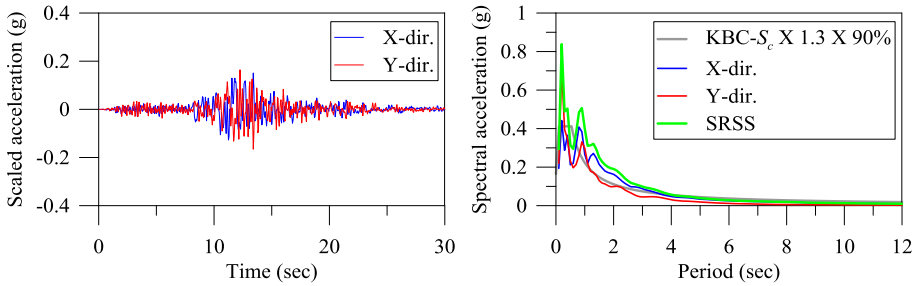

(b) DBE EQ2 Loma Prieta – SF – Pacific Heights

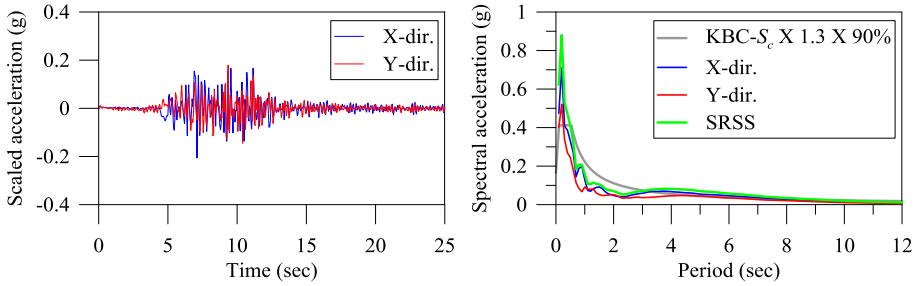

(c) DBE EQ3 Kocaeli – Gebze

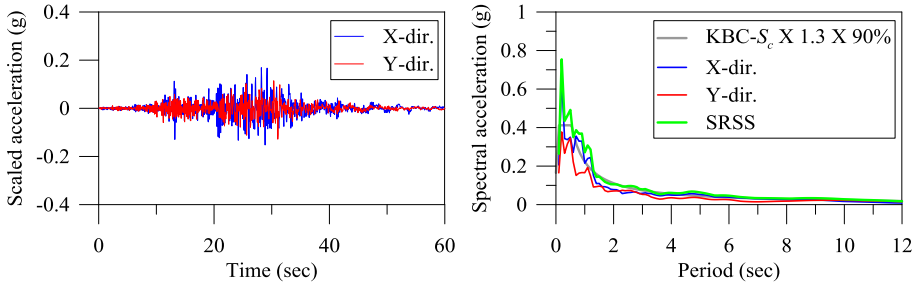

(d) DBE EQ4 Chi-Chi – ILA015

Figure 4-3 Ground motions records and response spectra of DBE (continued)

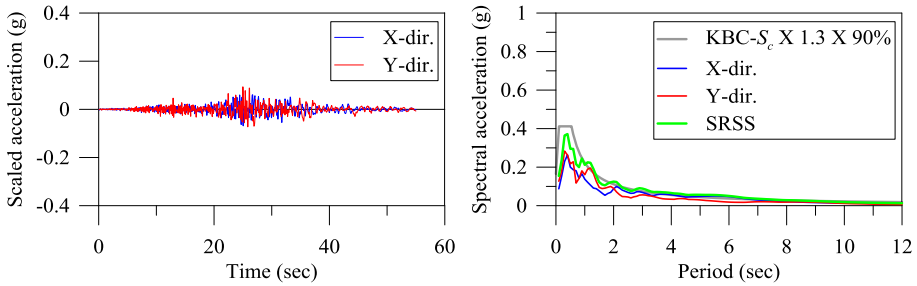

(e) DBE EQ5 Chi-Chi – TAP067

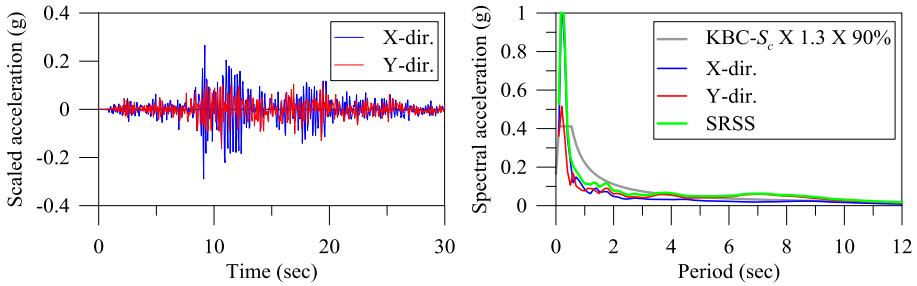

(f) DBE EQ6 Duzce – Lamont 1060

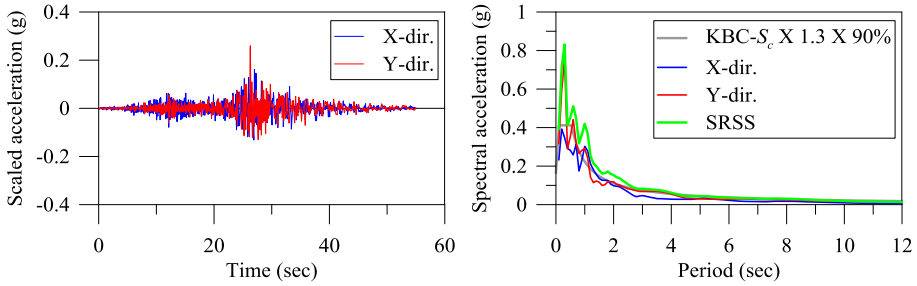

(f) DBE EQ7 Chi-Chi – TAP075

Figure 4-3 Ground motions records and response spectra of DBE

4.2 Maximum Considered Earthquake (MCE) records

4.2.1 Response spectrum of MCE

The maximum considered earthquake level is the earthquake with 2% probability of occurrence in a 50-year-exposure period. The maximum considered earthquake spectral acceleration for short periods, S_{MS}, and the Maximum Considered Earthquake spectral acceleration for 1-second period, S_{M1}, are 1.5 times S_{DS} and S_{D1}, respectively. The target response spectrum of MCE is shown in **Figure 4-4**.

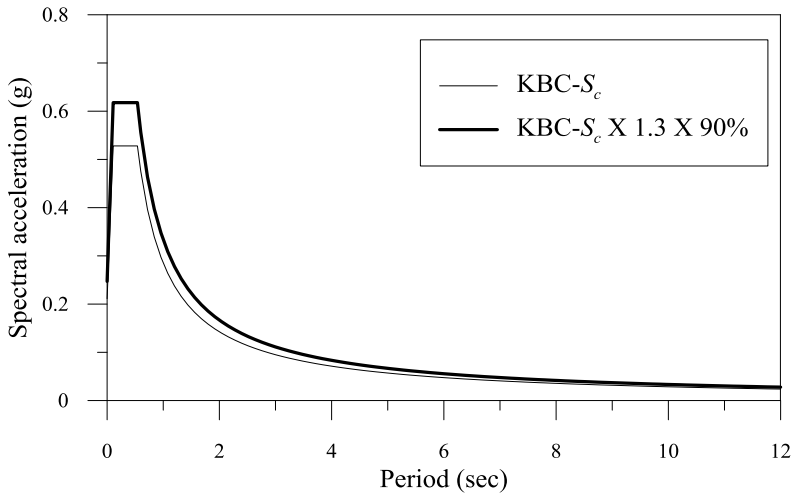

Figure 4-4 Response spectra of MCE

4.2.2 Ground motion records of MCE

The same ground motion records in **Table 4-1** are scaled to match the target spectrum of MCE level. The average SRSS response spectrum of scaled MCE ground motion is shown in **Figure 4-5**. **Figure 4-6** shows each MCE ground motion record and response spectrum of the record.

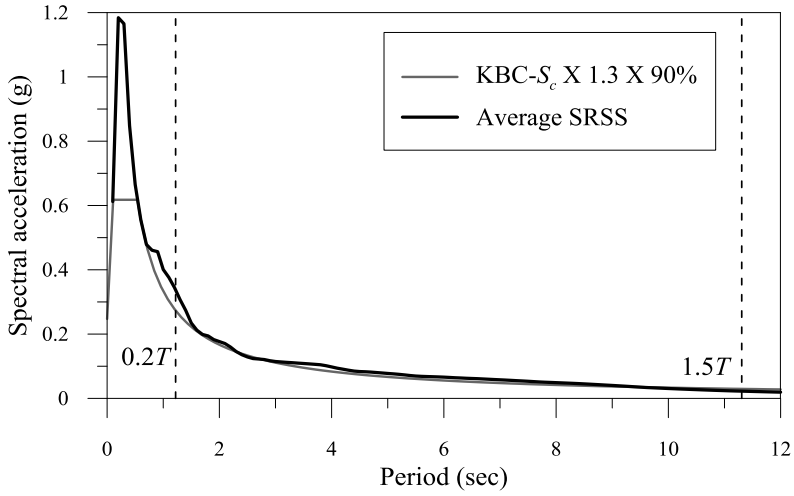

Figure 4-5 Average SRSS response spectrum of scaled MCE ground motions

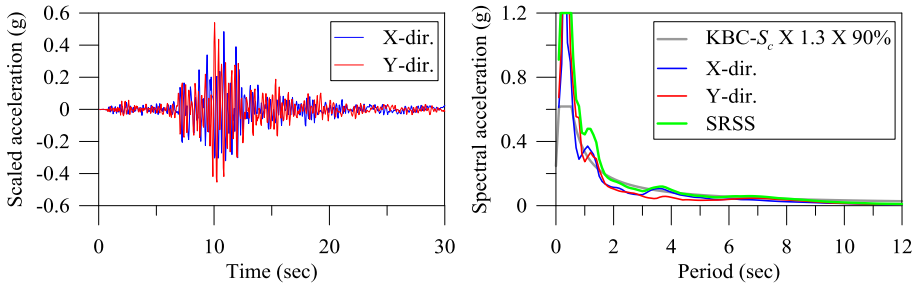

(a) MCE EQ1 Loma Prieta - Piedmont Jr High School Grounds

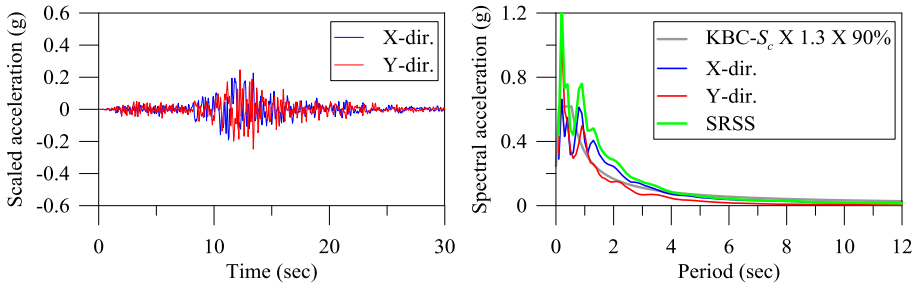

(b) MCE EQ2 Loma Prieta – SF – Pacific Heights

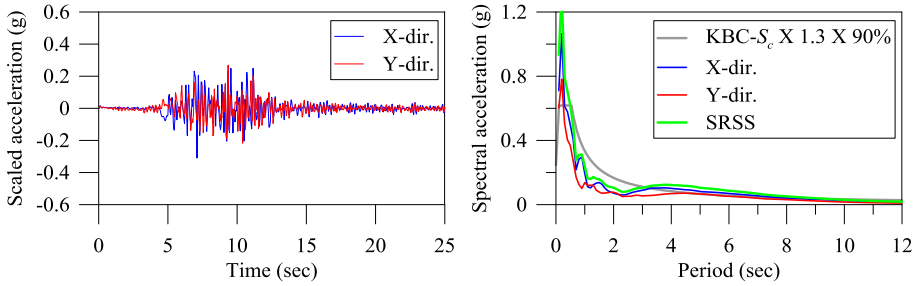

(c) MCE EQ3 Kocaeli – Gebze

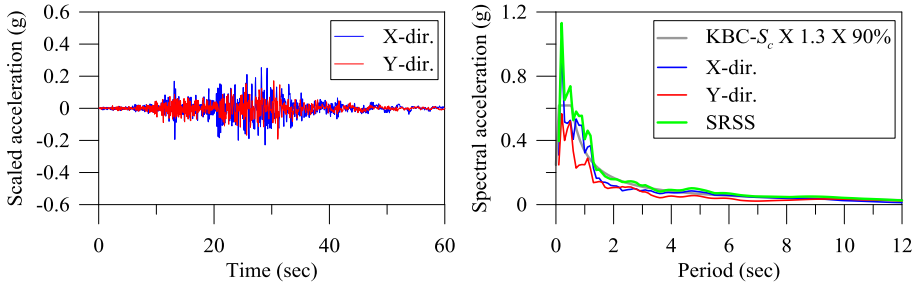

(d) MCE EQ4 Chi-Chi – ILA015

Figure 4-6 Ground motions records and response spectra of MCE (continued)

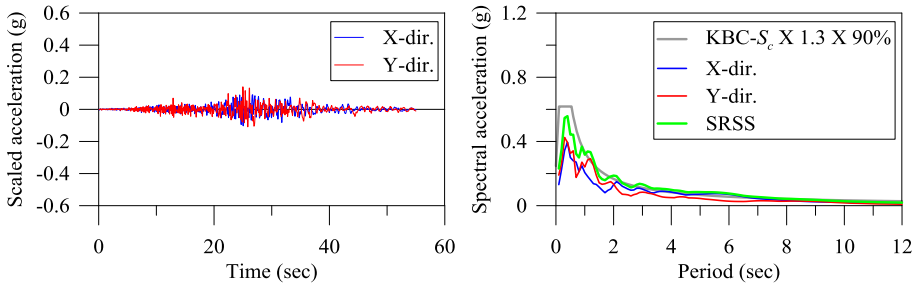

(e) MCE EQ5 Chi-Chi – TAP067

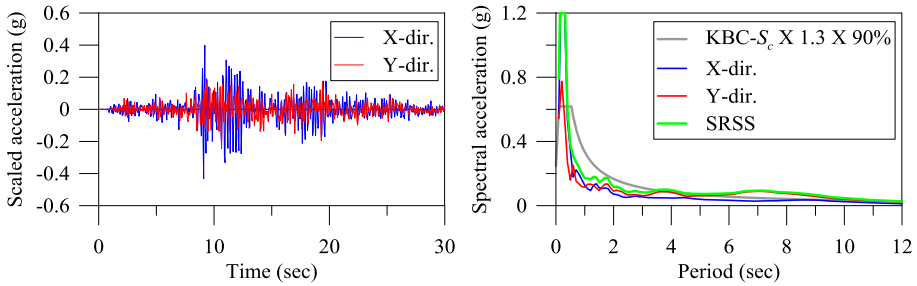

(f) MCE EQ6 Duzce – Lamont 1060

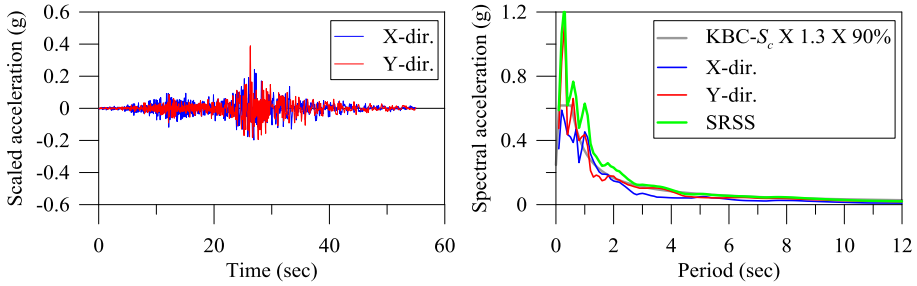

(f) MCE EQ7 Chi-Chi – TAP075

Figure 4-6 Ground motions records and response spectra of MCE

Chapter 5. Nonlinear Static Analysis

In this chapter, a set of nonlinear static analysis, called as the pushover analysis, are conducted. The seismic performance of the building is evaluated based on the nonlinear static analysis. Two guidelines, ASCE 41-13 and FEMA 440, are used for the seismic performance evaluation.

5.1 Load set

Before conducting the pushover analysis, a nonlinear static analysis for gravity loads is conducted for the initial condition of the pushover analysis. The load combination of expected gravity loads from the Guidelines for Performance-Based Seismic Design of Residential Buildings (2015) is used. The expected gravity load combination is determined by the following equation.

$$\text{Expected gravity load} = 1.0\ (\text{dead load}) + 0.25\ (\text{live load}) \qquad (5\text{-}1)$$

The force distributions for the 1^{st} mode in X- and Y-directions are used for equivalent static force distribution in X- and Y-directions, respectively. The displacement control method is used for the analysis. The monitored displacement is the center of the mass at the roof, which is recommended by the nonlinear static procedure in ASCE 41-13. The analysis model is pushed by 20 mm until the building collapses. The P-delta effect is considered.

5.2 Analysis results

5.2.1 X-dir. pushover analysis results

The pushover curve of X-direction is shown in **Figure 5-1**. The failure of members occurs at the total building drift of 1.24%, and the analysis is stopped due to the convergence problem. The first yielding occurs at the CB2 coupling beams of 27th and 28th floors with the total building drift of 0.26%. After the first yielding, the plastic hinges of coupling beams spread sequentially to the upper and lower parts from the outrigger wall floor due to the load redistribution. Although coupling beams yield earlier than columns and walls, the critical members are perimeter columns at B1st, 1st and 27th floors. The strain of concrete fibers of C05 and C06 columns at B1st and 1st exceed 0.002, which leads to the entire collapse of the building.

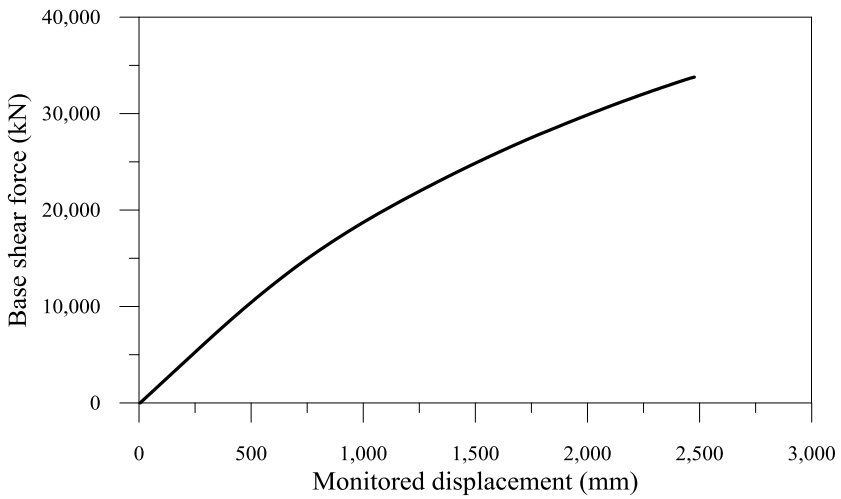

Figure 5-1 X-dir. pushover curve

5.2.2 Y-dir. pushover analysis results

Because the building is asymmetric about the X-direction, the pushover analyses for the Y-direction are conducted for the both of positive and negative directions. The results are shown in **Figure 5-2**. In case of Y-direction pushover analysis, the monitored displacement does not start from zero due to the differential column shortening. The perimeter columns have less stiffness compared to shear walls, and deform more in vertical direction under gravity loads, which leads to the lateral displacement at the roof.

The initial yielding occurs at the CB3 coupling beams of 49th floor in both of positive and negative direction pushover at the total building drift of 0.33% and 0.42%, respectively. The range of coupling beams where plastic hinges occurs starts from the top and mid-to-low floors and spreads to the 28th outrigger walls floor due to the load redistribution.

The building shows different ductility under positive and negative pushover; total building drift of 2.90% for positive direction and 1.24% for negative direction. In the positive direction pushover, the core walls resist the compressive force induced by overturning moment of the building. Because the core walls have a large thickness of 1,200 mm, the stress and strain of concrete fibers are not large, leading to ductile behavior of the building. On the other hand, the building shows less ductility in the negative direction pushover. The perimeter columns resist the compressive force due to the overturning moment. And the strain of concrete fibers of C01 and C02 columns at B1st and 1st floors exceeds 0.002.

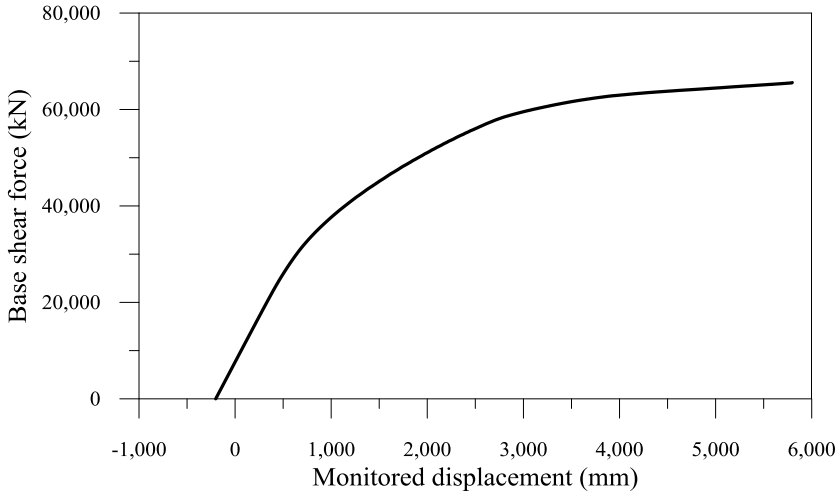

(a) Positive direction pushover curve

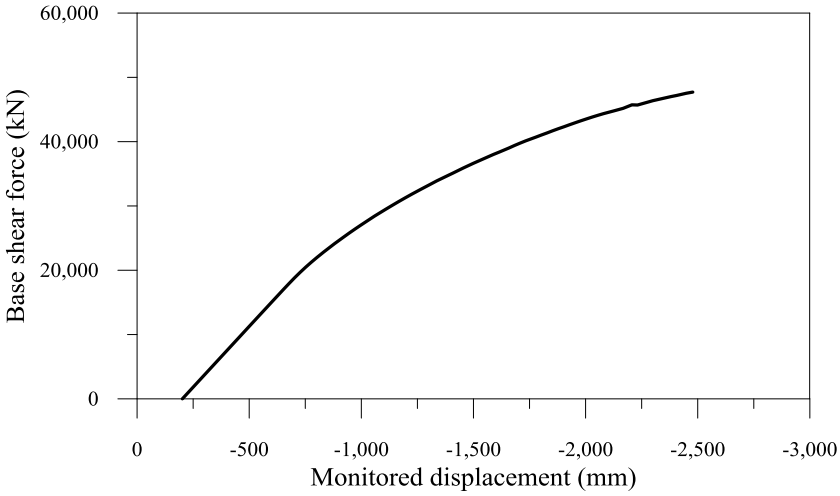

(b) Negative direction pushover curve

Figure 5-2 Y-dir. pushover curve

5.3 Performance evaluation

Although the seismic performance evaluation by a nonlinear static analysis has many limitations, it has been commonly used to reduce computational efforts until the performance of computers and analysis software improved. Seismic performance evaluation methods by nonlinear static analysis have been studied for a long time. Because the dynamic effects and hysteretic behavior of members cannot be considered in a nonlinear static analysis, there are many parameters to consider those in the seismic performance evaluation procedure by a nonlinear static analysis. In this section, the seismic performance evaluations are conducted by two guidelines, ASCE 41-13 and FEMA 440.

5.3.1 ASCE 41-13 target displacement

The seismic performance evaluation method of ASCE 41-13 nonlinear static procedure, which is called as the coefficient method, is based on target displacement. The target displacement is determined using idealized pushover curve and modification factors, and the seismic performance is evaluated based on when the lateral displacement of the building is the target displacement. The target displacement, δ_t, is determined by the following equation.

$$\delta_t = C_0 C_1 C_2 S_a \frac{T_e^2}{4\pi^2} g \tag{5-2}$$

where

C_0: modification factor for converting the roof displacement of multi-degree-of-freedom system to the spectral displacement of equivalent single-degree-of-freedom system.

C_1: modification factor for expected maximum inelastic displacement, C_1 =1.0 for periods larger than 1.0s.

C_2: modification factor for hysteretic behavior, C_2 =1.0 for periods larger than 0.7s.

S_a: response spectral acceleration at the effective fundamental period.

T_e: effective fundamental period.

The effective fundamental period is determined by the following equation.

$$T_e = T_i \sqrt{\frac{K_i}{K_e}} \tag{5-2}$$

where

T_i: elastic fundamental period.

K_i: elastic lateral stiffness of the building.

K_e: effective lateral stiffness of the building determined by the idealized pushover curve.

The idealized pushover curve is shown in **Figure 5-3**. The modification factors, effective fundamental period, and target displacement are shown in **Table 5-1**.

Table 5-1 Target displacement

Load case	T_e (sec)	C_0	C_1	C_2	DBE δ_t (mm)	MCE δ_t (mm)
X-dir.	7.89	1.5	1	1	559.2	841.7
Y-dir. positive	6.98	1.5	1	1	293.2	543.4
Y-dir. negative	7.09	1.5	1	1	704.6	958.6

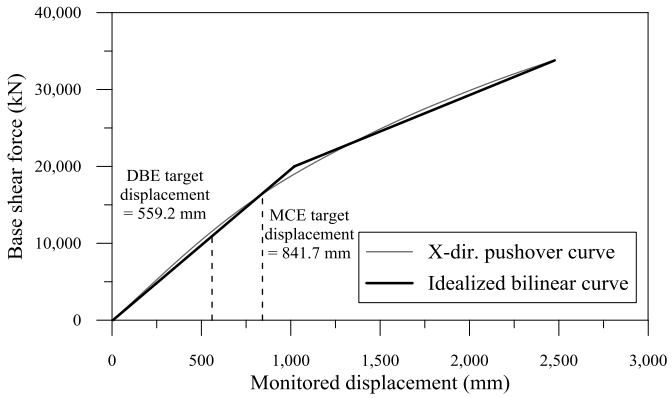

(a) X-dir. pushover curve and idealized curve

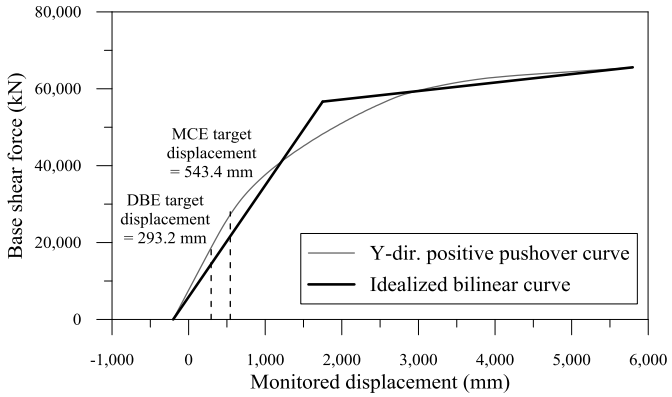

(b) Y-dir. positive pushover curve and idealized curve

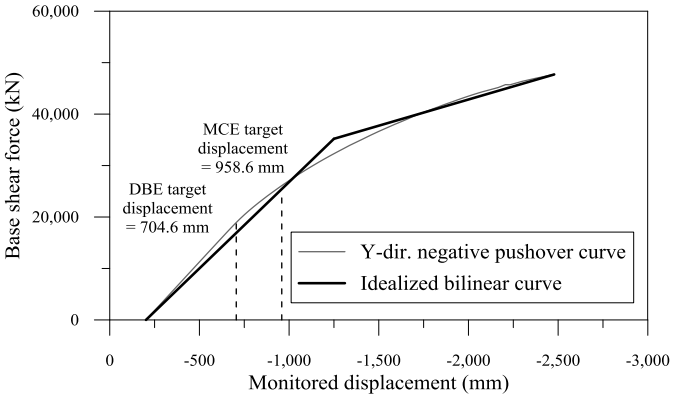

(b) Y-dir. negative pushover curve and idealized curve

Figure 5-3 Idealized bilinear curve and target displacement

The building states at the target displacement of DBE are almost elastic. In case of X-direction pushover, only the CB2 coupling beams at the 27th and 28th floors yield, and the plastic rotations are less than 0.01%. In case of both of positive and negative Y-direction pushover, there are no yield members at the target displacement.

The yield range of coupling beams increases at the target displacement of MCE. In case of X-direction pushover, the CB2 coupling beams yield from the 8th to 24th, 27th to 42nd, and 47th to 49th floors, and other members are elastic. The maximum plastic rotation of CB2 is 0.07% which is almost negligible. For the positive Y-direction pushover, the whole members are also elastic at the target displacement of MCE. In case of negative Y-direction pushover, CB3 from the 47th to 49th floors yield, and the plastic rotations are less 0.01%.

Although the main structural elements can afford to resist more seismic loads, nonstructural elements can be damaged under the large interstory drift. The acceptance criteria of the interstory drift are commonly used for the seismic performance evaluation of the global system. **Table 5-2** is the acceptance interstory drift criteria of the building with concrete walls suggested by FEMA 356.

Table 5-2 Interstory drift limits of concrete walls in FEMA 356

Drift	Structural performance levels		
	Immediate occupancy (IO)	Life safety (LS)	Collapse prevention (CP)
Transient	0.5%	1%	2%
Permanent	Negligible	0.5%	2%

Figure 5-4 and **Figure 5-5** shows the intersotry drift at the DBE and MCE target displacement.

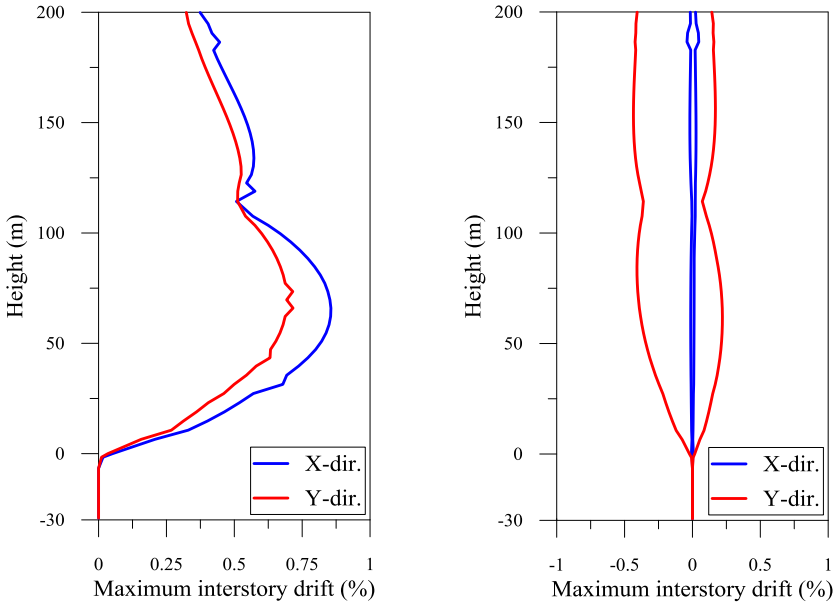

(a) X-dir. pushover (b) Y-dir. pushover

Figure 5-4 Maximum interstory drift at the DBE target displacement

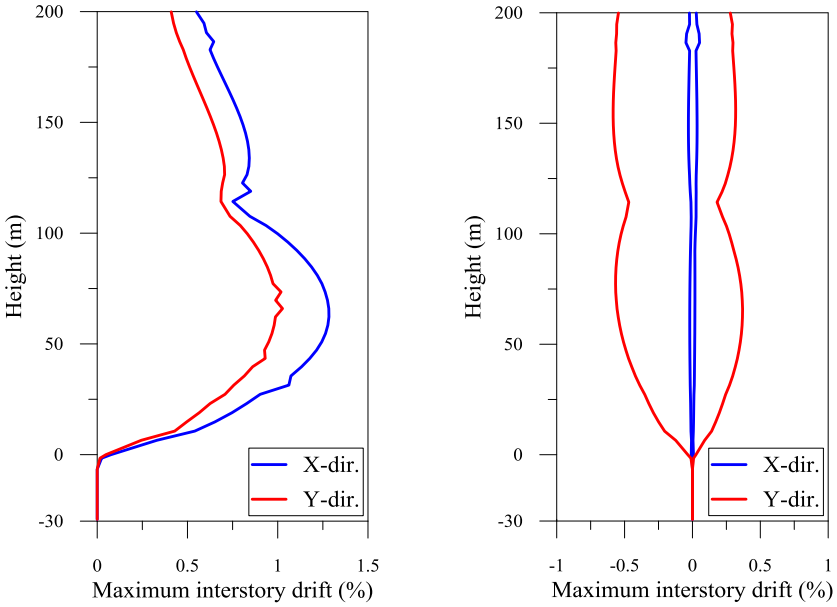

(a) X-dir. pushover (b) Y-dir. pushover

Figure 5-5 Maximum interstory drift at the MCE target displacement

From the interstory drift limits, the seismic performances according to the interstory drift are LS at the DBE target displacement and CP at the MCE target displacement.

5.4 Discussion

In this chapter, the nonlinear static analysis called as pushover analysis is conducted. The seismic performance evaluations are conducted by ASCE 41-13 and FEMA 440. The results are summarized as follows:

1) From the pushover analysis, the building shows different ductility capacity in X, positive Y, and negative Y-directions due to the asymmetric structural plan. The maximum roof drifts before the failure of members are 1.24% for X and negative direction, and 2.90% for positive direction.

2) The coupling beams yield earlier than vertical members. The locations of the first yield coupling beam of X-direction pushover are near the 28^{th} floor, where the outrigger walls exist, and the yield range spreads toward upper and lower stories. The locations of the initial yield coupling beams of Y-direction pushover are upper and mid-to-low floors, and the yield range spreads toward 28^{th} floor.

3) The collapse of building occurs due to the failure of concrete fibers of columns at the 1^{st} and 1^{st} floors. In case of negative Y-direction pushover, the perimeter columns, C01 and C02, resist the compression force due to overturning moment of the building, and the concrete fibers fail earlier. On the other hand, the massive core wall resist the compression force in the positive Y-direction pushover, and the building shows larger roof drift of 2.90%.

4) From the seismic performance evaluation of ASCE 41-13, the building remains in almost elastic range at the target displacement. Only the coupling beams at 27^{th} and 28^{th} floor yield in the X-direction pushover, and the plastic rotations are less than 0.01%. It means the seismic performance of the building under DBE is the immediate occupancy (IO).

Chapter 6. Nonlinear Time History Analysis

In this chapter, nonlinear integration time history analyses are conducted using DBE and MCE level ground motion records. The seismic performances of the building under both of DBE and MCE ground motion records are evaluated. The seismic performance of members is evaluated in accordance with ASCE 41-13.

6.1 Load set

The gravity loads are set as the initial condition of the nonlinear time history analysis in the same manner of the pushover analysis. The ground motions in Chapter 4 consist of a pair of one component and perpendicular component. A pair of ground motion records consisting of two components is applied at the same time.

For the time integration, the Hilber-Hughes-Taylor (HHT) method which is an extension of Newmark's integration method is used. The HHT method has an additional parameter of α to control the numerical dissipation. The α parameter is from -1/3 to 0, and when α is zero the HHT method is the same as Newmark's integration with β and γ parameters of 0.25 and 0.5, respectively. According to the research by Broderick et al. (1994), the numerical dissipation of HHT method is governed by the time step and period of mode. From their paper, the modes whose periods are larger than 8 times the time step are not affected by the numerical dissipation. And the modes whose periods are less than 4 times the time step are damped out when α is equal or less than -0.1. In this study, α of -1/3 and time step of 0.05 seconds are used to reduce computational efforts. It means the effects of higher order mode with periods less than 0.2 seconds are damped out. Because the periods of from the 20^{th} modes are less than 0.2 seconds, the effect of numerical

dissipation is not large.

In order to confirm the effects of the numerical dissipation in this model, the results of the analyses when the α is 0 and -1/3 are compared. For the comparison, the analyses are conducted using the MCE ground motion records of EQ1 Loma Prieta. The EQ1 has the strongest high-frequency components. **Figure 6-1** shows the comparison of the results.

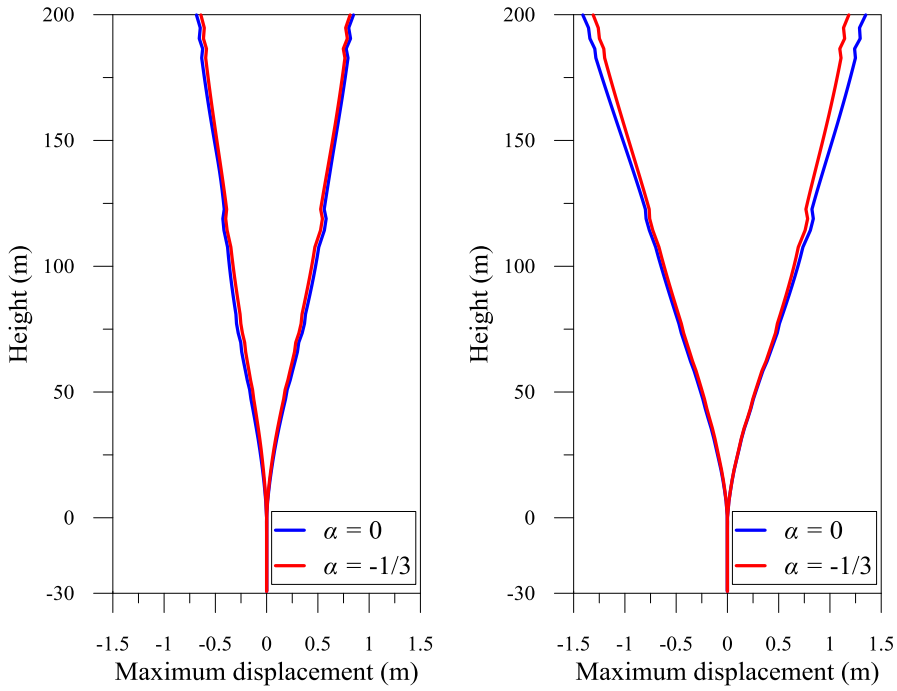

(a) X-direction (b) Y-direction

Figure 6-1 Maximum displacement under MCE EQ1

The use of α of -1/3 reduces the response due to the numerical dissipation. In case of the result of MCE EQ1, the effect of the numerical dissipation in Y-direction is relatively large, and the difference increases along the height. The reason that the difference of Y-direction is larger than X-direction appears to be related to the effect of torsion. The torsion of the T-shape building causes additional Y-direction deformation under the X-direction forces. The

maximum difference at the roof is about 12%.

Although there are a little difference between the results when the values of α of 0 and -1/3 are used, the influence of the numerical dissipation in the periods less than 0.4 seconds is acceptable considering the excessive peak in the high-frequency range in the average response spectrum of the input ground motions. The use of α of -1/3 reduces the analysis time to less than half that of α of 0. Therefore, the HHT method with α of -1/3 is used to reduce the computational efforts in this study.

6.2 Analysis results and performance evaluation of DBE

From the KBC 2016, the seismic performance of time history analysis can be evaluated using the average responses of ground motions when more than 7 ground motions are used. Thus, the evaluation of seismic performance under DBE ground motion records is conducted using the average responses.

6.2.1 Maximum displacement and interstory drift

The maximum displacement and interstory drift along the height of the building under the 7 DBE ground motions are shown in **Figure 6-2**. As shown in **Figure 6-2**, the average response of Y-direction interstory drifts exceed 0.5%, and the building satisfies the performance level of LS under DBE in accordance with FEMA 356. The interstory drifts of negative Y-direction are relatively larger due to the initial lateral displacement due to gravity loads. And the interstory drifts of stories upper than the 28^{th} floor are not large. It seems that the outrigger walls significantly contribute to reducing the lateral displacement.

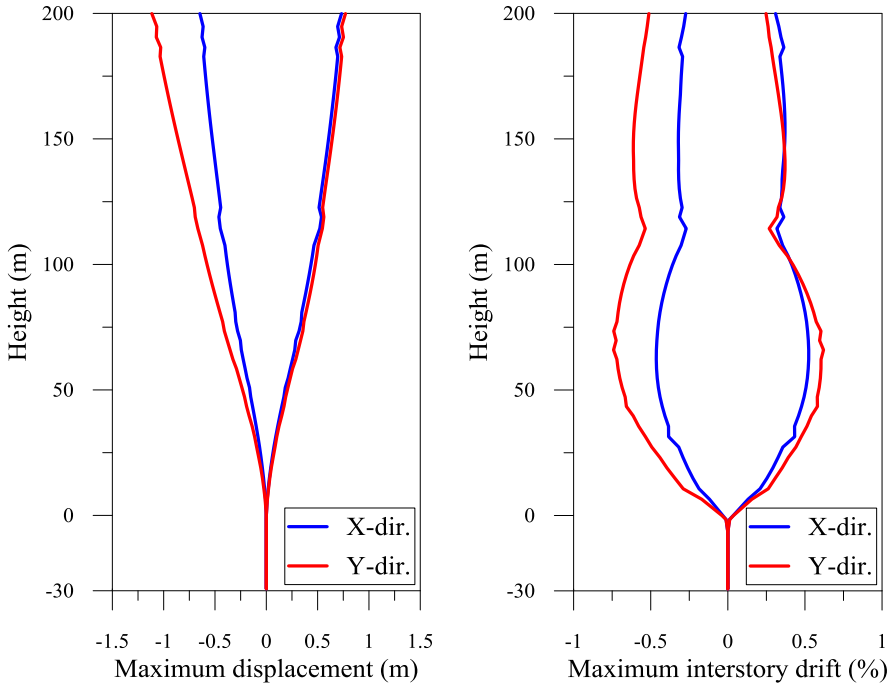

(a) Maximum displacement (b) Maximum interstory drift

Figure 6-2 Average responses of the 7 DBE ground motions

6.2.2 States of nonlinear hinges and fiber elements

The seismic performance of the building should be also evaluated for the individual members. In this study, the seismic performance of individual members is evaluated in accordance with ASCE 41-13.

As expected, the vertical members remain elastic, and only the coupling beams are reached to the yield under the DBE seismic loads. From the analysis results, the responses of nonlinear dynamic analysis seem to be significantly affected by the characteristics of the ground motion. The yield ranges of coupling beams vary depending on the ground motions. The yielding of CB1 primarily occurs at the upper part of the building under the ground motions of EQ2, EQ4 and EQ5 which mainly have strong high-

frequency components. The yielding of CB3 occurs from mid to top of the building under the ground motions of EQ3 and EQ6 which have strong low-frequency components.

The average states of nonlinear hinges assigned to the coupling beams are shown in **Figure 6-3**. The maximum plastic chord rotations of the coupling beams do not exceed 0.1%, which is negligible. All of the coupling beams satisfy the IO performance level in ASCE 41-13 under the 7 DBE ground motion.

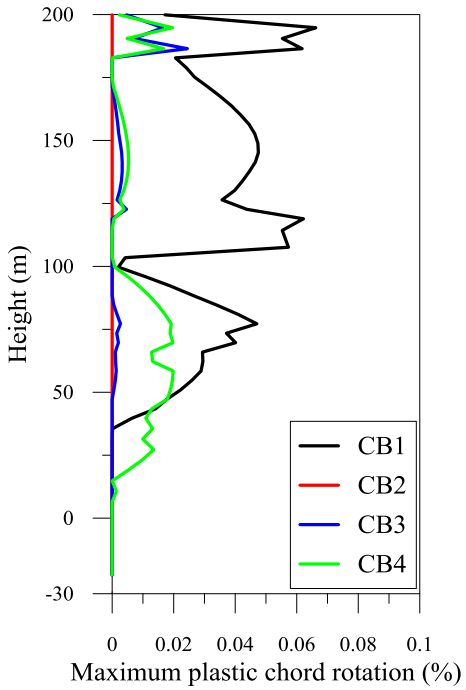

Figure 6-3 Average of the maximum plastic chord rotations of coupling beams

Although the plastic rotations of coupling beams are negligible, the range of plastic rotation is much larger than that at the target displacement or performance point of the nonlinear static analysis. The location of plastic hinge is also different from the nonlinear static analysis. The CB2 coupling beams are expected to yield first in the nonlinear static analysis, but CB2

coupling beams are kept to be elastic in the nonlinear time history analysis. This seems to be due to the effects of the higher order modes in the nonlinear dynamic analysis. The torsional forces induced by higher order modes make the CB1 coupling beam be critical members. The X-direction excitation induces Y-direction forces due to asymmetric plan about the X-direction, and the yield range of the CB3 coupling beams increases compared to that of nonlinear static analysis.

6.3 Analysis results of MCE

6.3.1 Maximum displacement and interstory drift

The maximum displacement and interstory drift along the height of the building under the 7 MCE ground motions are shown in **Figure 6-4**. The pattern of the interstory drift along the height is similar to that of DBE, but the values are much larger. The average responses of Y-direction interstory drifts exceed 1.0%, and the building satisfies the performance level of CP under MCE in accordance with FEMA 356.

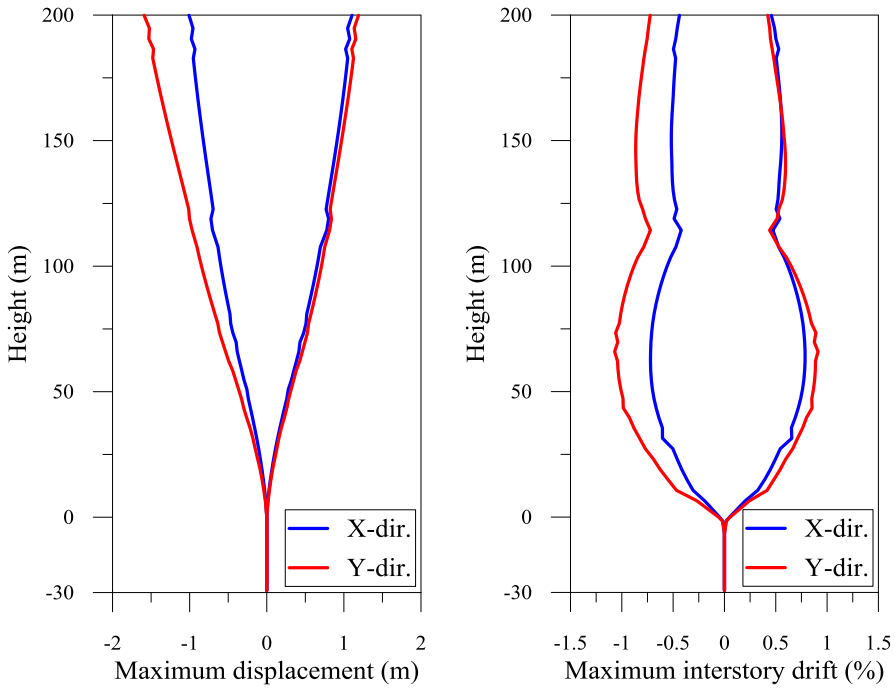

(a) Maximum displacement (b) Maximum interstory drift

Figure 6-4 Average responses of the 7 MCE ground motions

6.3.2 States of nonlinear hinges and fiber elements

The average states of nonlinear hinges assigned to the coupling beams under MCE ground motions are shown in **Figure 6-5**. The maximum plastic chord rotations of the coupling beams are much larger than that of DBE ground motions. However it does not exceed 0.5%, and all of the coupling beams satisfy the IO performance level in ASCE 41-13 under the 7 DBE ground motion.

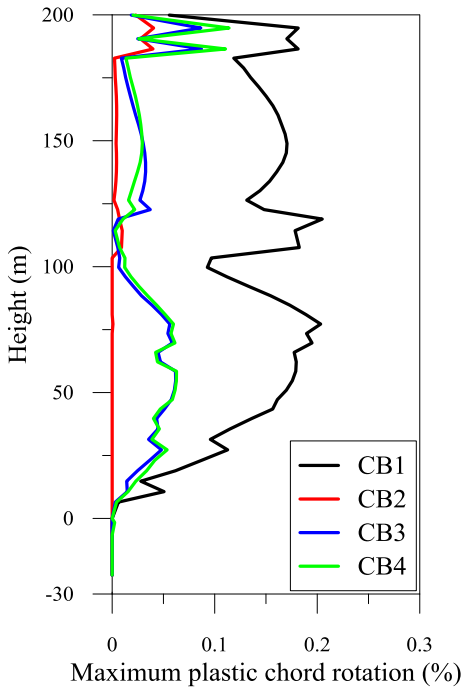

Figure 6-5 Average of the maximum plastic chord rotations of coupling beams

All of the vertical elements are also kept to be elastic under MCE ground motions. However, the maximum compressive strain of concrete fibers of C01 and C02 exceeds 0.0015. It can be critical under stronger seismic loads, because the concrete fibers are assumed to be unconfined and the strength of concrete fiber drops quickly after the strain of 0.002.

6.4 Influence of the outrigger walls

The outrigger walls at the 28th floor are used to satisfy the building drift of H/600 under serviceability wind loads. It transfers the overturning moment to the perimeter columns, which induces the axial forces at the perimeter columns. In the Y-direction, the concrete fibers of perimeter columns near the ground level are expected to reach a strain of 0.002 before the failure of coupling beams, which leads to the brittle failure of the entire building. The use of outrigger walls can reduce the lateral displacement under wind loads, but also can reduce the ductility of the building under seismic load. Therefore, an attention is required to the use of outrigger walls in a high-rise building and the application of the confinement at the columns near the ground level also may be required.

6.5 Influence of modeling of underground structure

Aforementioned, the results depending on the basement modeling methods are compared in this section. For the comparison, the MCE ground motion records of the EQ1, EQ2, and EQ3 are used because the characteristics of each ground motion are unique. The EQ1 has very strong short period components and the EQ3 has very strong long period components. The response spectrum of EQ2 is very close to the target MCE response spectrum of KBC 2016.

6.5.1 Maximum displacement

The comparisons of the maximum displacement are shown in **Figure 6-6** to **Figure 6-8**. The original model is the laterally supported model, and the comparison model is the model including the surrounding underground parking lot without considering the soil-structure-interaction.

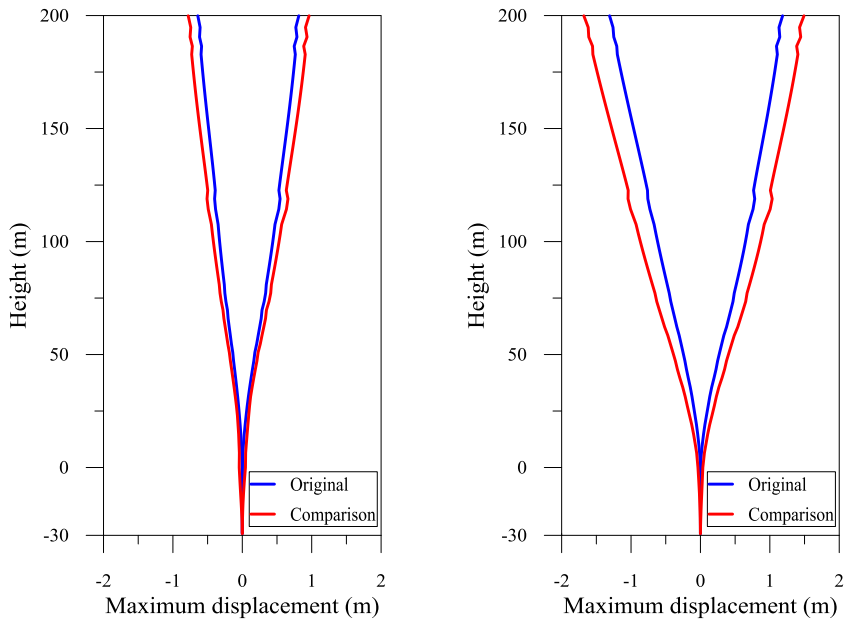

(a) X-direction (b) Y-direction

Figure 6-6 Maximum displacement comparison under EQ1

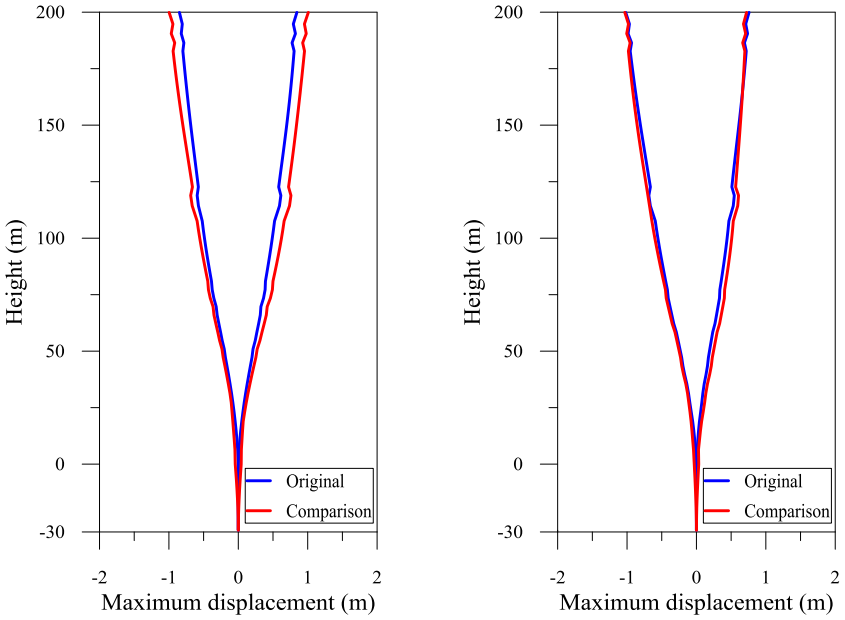

(a) X-direction (b) Y-direction

Figure 6-7 Maximum displacement comparison under EQ2

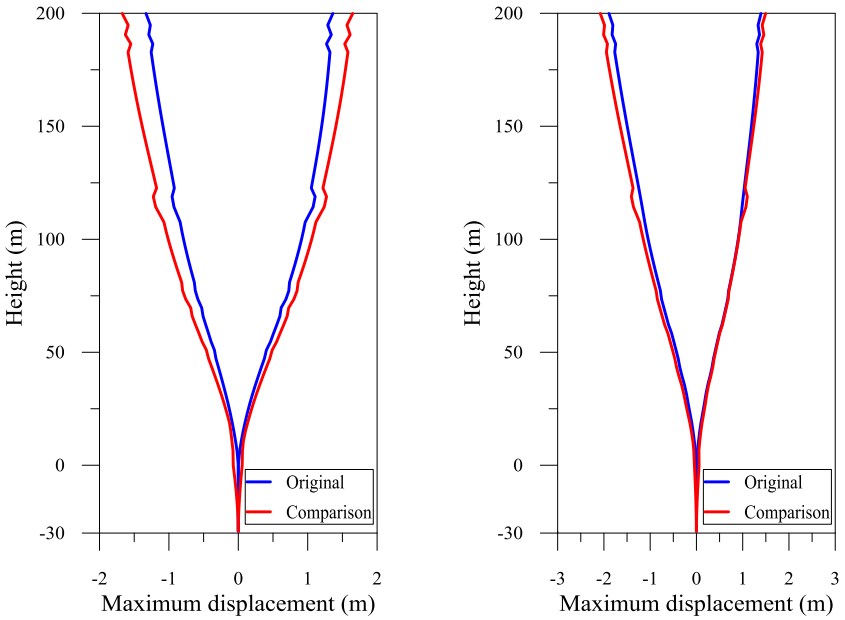

(a) X-direction (b) Y-direction

Figure 6-8 Maximum displacement comparison under EQ3

As shown in **Figure 6-6** to **Figure 6-8**, there are differences between the results of the two models. Because the model with surrounding parking lot is not laterally supported, there are lateral displacements at the underground structures. So the lateral displacement of the comparison model is larger than that of the laterally supported basement model.

6.5.2 Plastic rotation of coupling beams

The plastic chord rotations of coupling beams from the two models are shown in **Figure 6-9** to **Figure 6-11**.

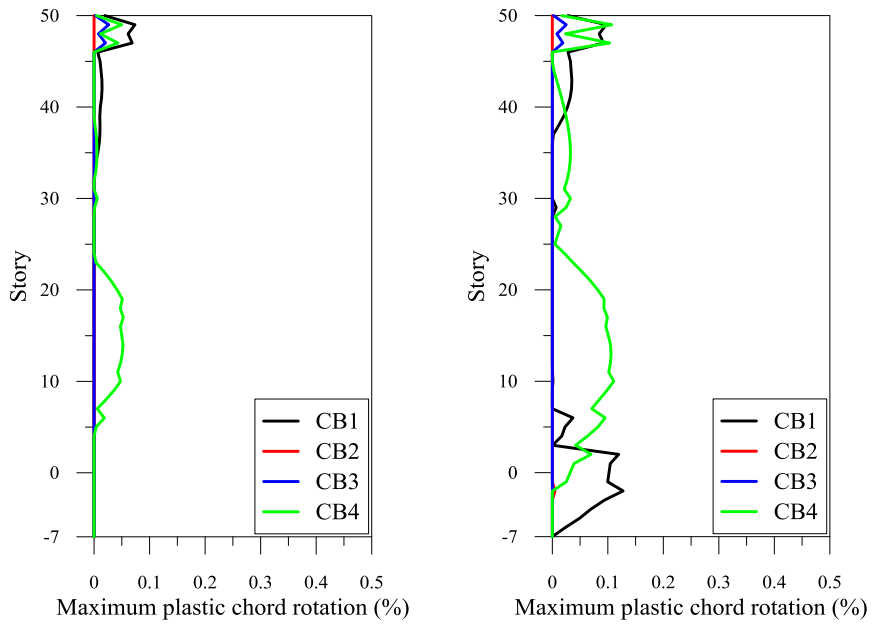

(a) Original model (b) Comparison model

Figure 6-9 Comparison of maximum plastic rotation of coupling beam under EQ1

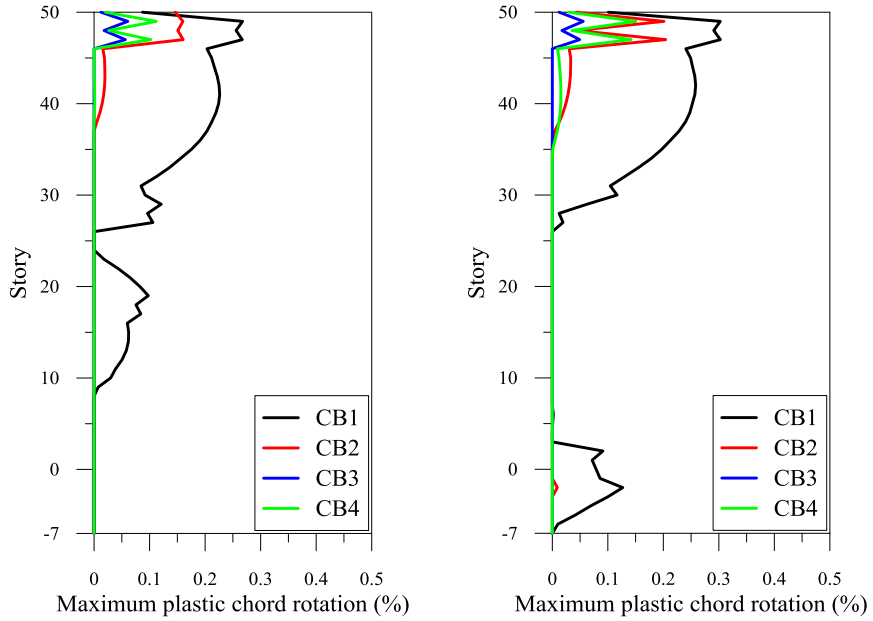

(a) Original model (b) Comparison model

Figure 6-10 Comparison of maximum plastic rotation of coupling beam under EQ2

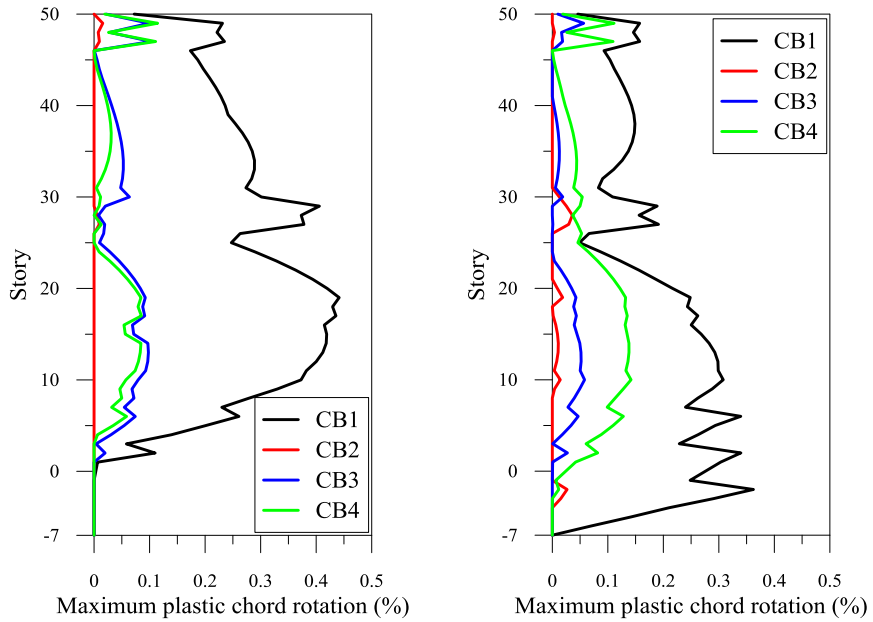

(a) Original model (b) Comparison model

Figure 6-11 Comparison of maximum plastic rotation of coupling beam under EQ3

Based on the results, the yielding of CB1 coupling beams at the underground occurs in the comparison model, which induces the difference of plastic rotation distribution patterns along the height.

6.5.3 Core wall shear forces near the ground level

The shear forces of core walls of the two models under the MCE EQ1 are shown in **Table 6-1**. The IDs of the core walls are shown in **Figure 3-2**.

Table 6-1 Comparison of core wall shear forces

Core wall	Core wall shear forces (kN)							
	Original model				Comparison model			
	2F	1F	B1F	B2F	2F	1F	B1F	B2F
CW1	5,096	6,700	19,237	2,280	5,307	5,690	6,263	7,505
CW2	10,374	10,410	32,084	8,875	10,103	9,750	14,007	18,011
CW3	2,965	4,722	8,432	2,519	3,067	2,572	3,846	2,775
CW4	8,462	7,899	21,149	6,875	7,008	6,748	8,040	11,324
CW5	7,811	8,068	21,927	5,564	7,351	6,821	5,613	6,494
CW6	13,528	14,048	41,508	10,157	11,783	12,478	10,419	13,132
CW7	6,095	6,688	24,326	4,509	8,958	6,013	5,714	7,324
CW8	10,478	9,673	41,178	9,202	12,831	7,615	10,610	15,125
Sum	64,808	68,209	209,839	49,979	66,406	57,686	64,511	81,688

As shown in **Table 6-1**, the shear force distribution above the ground level is hardly affected by the modeling of underground structures. However, it significantly affects the story shear distribution of the basement. If the whole underground structures are laterally supported, the story shear increases dramatically at the just below of the ground level, which seems not to be realistic. If there is no lateral support or spring in the basement model, the story shear is concentrated at the base, which may underestimate the back stay effect at the ground level. Therefore, the modeling of lateral soil springs is recommended; however, it is often difficult to determine the stiffnesses of soil springs. In case of using the nonlinear lateral springs for modeling the stiffness of the surrounding soil, the distribution of story shear depends on the

stiffness of the springs.

6.5.4 Discussion

In this section, the results depending on the basement modeling methods are compared. The results above the ground level are similar to each other. The difference is that an excessive shear force is observed at the $B1^{th}$ floor in the laterally supported model. The laterally supported model appears to overestimate the backstay effect. The results of the comparison model including surrounding parking lot without the soil-structure-interaction may be close to the actual behavior at the basement. However, computational cost is quite large to make the model and run the analysis. Although an exact modeling is recommended, considering the computational cost, a laterally supported model with the portion of the surrounding basement structures may be proper for a design practice.

6.6 Responses depending on the characteristics of ground motions

In the time history analysis, the responses of the building are significantly affected by the characteristics of the input ground motions. In this section, the responses of each MCE ground motion are compared. **Figure 6-12** to **Figure 6-18** show the response spectrum and the plastic rotation of selected coupling beams under each ground motion.

As shown in **Figure 6-12**, although the response spectrum of MCE EQ1 has the largest spectral acceleration at the periods less than 1 second, the range of yielding drift for coupling beams and the associated plastic rotations are less than those under other ground motions. The reason is that numerical dissipation due to the use of HHT method and Rayleigh damping reduces the effect of high-frequency components. The response spectra of MCE EQ2 and EQ4 seem to be similar to each other, but there is a large difference in the distribution of plastic rotation of CB1. Such a difference seems to be caused by the difference of response spectrum near the period of 5 seconds which is close to the period of the 3rd mode. The EQ4 has a slightly larger spectral acceleration at the period of 5 seconds than the EQ2. The 3rd mode is the torsion of the building, and it affects the rotation of CB1. From **Eq. 3-3**, the rotation of a coupling beam increases when the relative length of the core wall is long. Even if there is a similar deformation of core walls by the torsional force, the CB1 is connecting longer core walls than CB2, and deforms more than CB2.

The response spectrum of MCE EQ3 has the large spectral accelerations from the periods of 3 to 6 seconds. Like EQ4, the plastic rotation of CB1 is large due to the effect of torsion. The plastic rotations of CB3 and CB4 are also large due to 2nd mode with the period of 6.12 seconds.

In case of MCE EQ5, EQ5 has the lowest high-frequency components and no large response spectrum. However, the spectral accelerations at the periods

near 5 seconds are relatively large and the duration of the ground motion is long, which makes the largest plastic rotation of CB1.

The response spectrum of EQ6 is the largest at the periods from 6 to 8 seconds. The EQ6 also has large high-frequency components at the periods near 0.3 seconds. Due to the numerical dissipation, the effect of the high-frequency components is reduced, and the ground motion mainly affects the 1st and 2nd modes of the building. Due to the influence of the 2nd mode, large plastic rotations are observed in the CB3 and CB4.

In case of the EQ7, EQ7 has large high-frequency components, and the yield of coupling beams occurs at the upper parts of the building due to the influences of the higher order mode.

From the responses of each ground motion, it is turned out that the effect of the 3rd mode which causes torsional forces much affects significantly when the response spectrum of a ground motion has the large spectral acceleration at the period of the 3rd mode. Other modes are not affected sensitively by the characteristics of the ground motions compared to the 3rd mode. It seems to be due to the Rayleigh damping. The 3rd mode has 1.68% damping ratio which is 16% less than that of fundamental period. The 4th mode also has 1.73% damping ratio, but the mass participation ratio is much less than the 3rd mode.

In all cases, the plastic rotations of coupling beams decrease from the 25th to 27th floors, because the same details of coupling beams are used from 20th to 27th floors. Therefore, an optimized design is required for this part. The peak of plastic rotations is also observed from the 28th to 30th floors. There are outrigger walls at the 28th floor and thicker slabs are used from the 28th to 30th floors. The lateral stiffness of other elements is relatively larger, but the longitudinal reinforcements of the coupling beams are significantly reduced compared to the 27th floor due to the design optimization, resulting in the largest plastic rotations at the 28th to 30th floors. The second largest plastic

rotation is also observed near the roof, because the size of coupling beams is reduced from the 48th floor.

There is a tendency that the strong high-frequency components of a ground motion induce very large plastic rotations of coupling beams at the upper parts of the building, and the strong low-frequency components increase plastic rotations at the lower parts. Although the Demand-Capacity Ratios (DCR) of coupling beams which is governed by wind loads are similar along the height, there is a difference of the vertical load distribution between the wind loads and seismic loads. Thus, the yield ranges and plastic rotations of coupling beams are different depending on the governing modes in the time history seismic analysis.

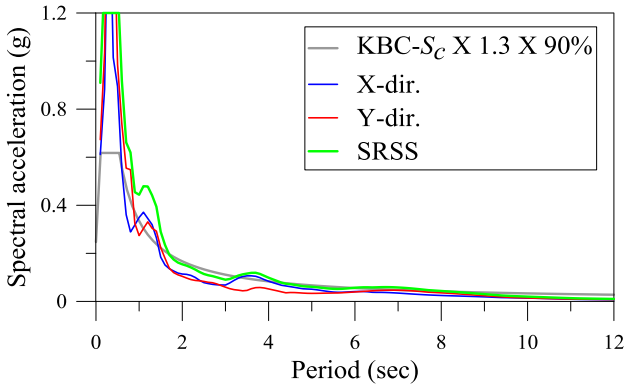

(a) Response spectrum

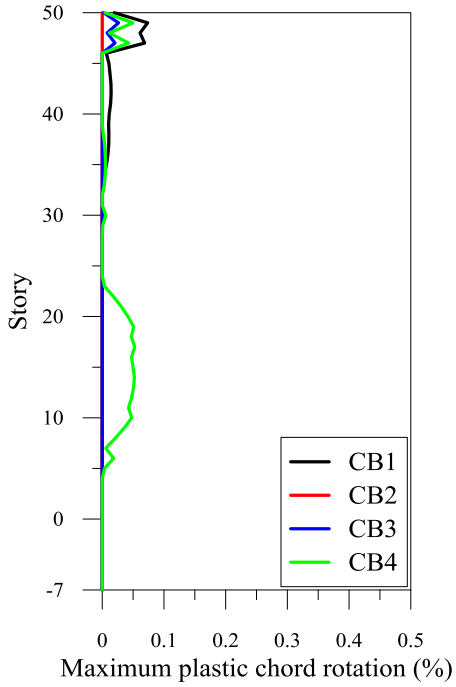

(b) Maximum plastic rotation of coupling beams

Figure 6-12 Response spectrum and maximum plastic rotation of MCE EQ1

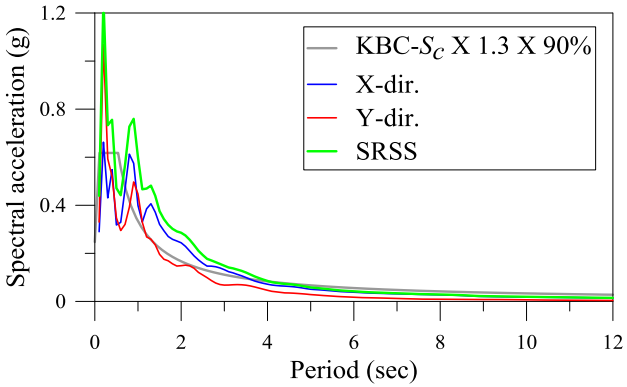

(a) Response Spectrum

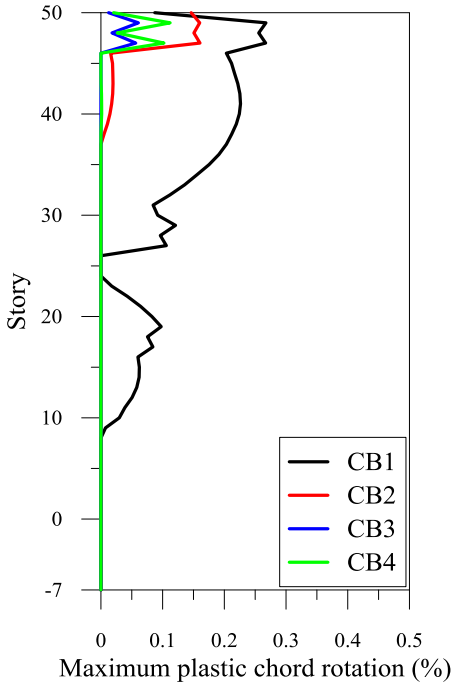

(b) Maximum plastic rotation of coupling beams

Figure 6-13 Response spectrum and maximum plastic rotation of MCE EQ2

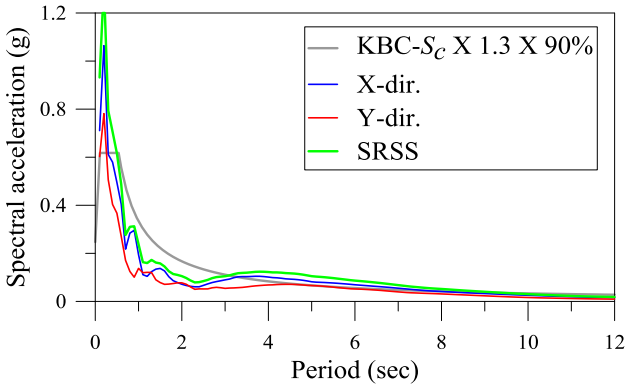

(a) Response spectrum

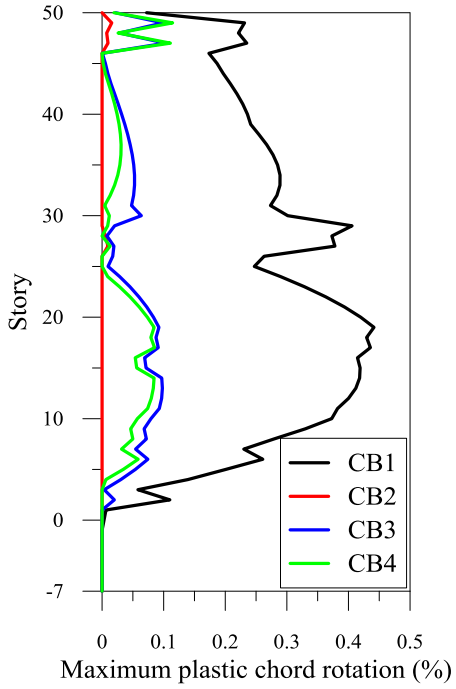

(b) Maximum plastic rotation of coupling beams

Figure 6-14 Response spectrum and maximum plastic rotation of MCE EQ3

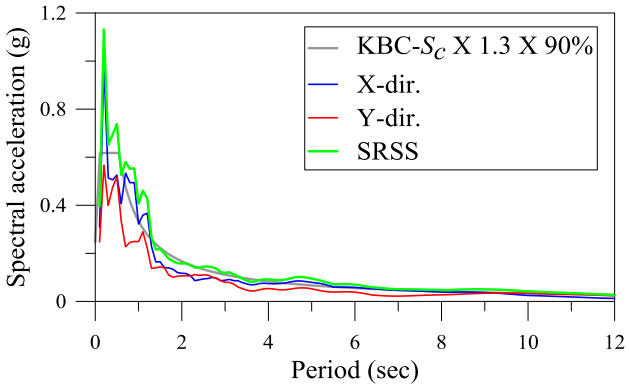

(a) Response spectrum

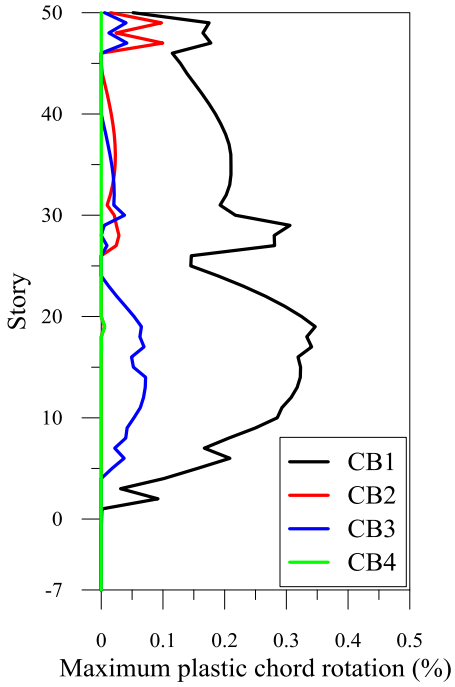

(b) Maximum plastic rotation of coupling beams

Figure 6-15 Response spectrum and maximum plastic rotation of MCE EQ4

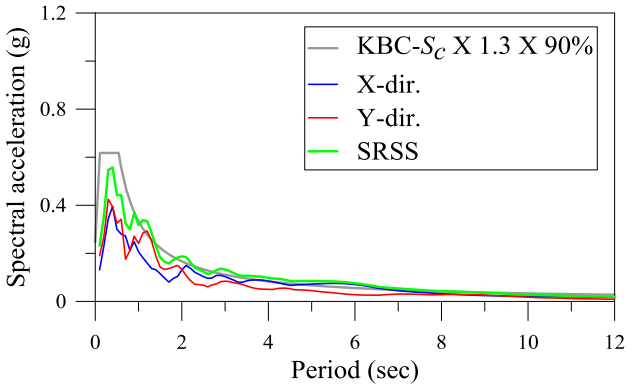

(a) Response spectrum

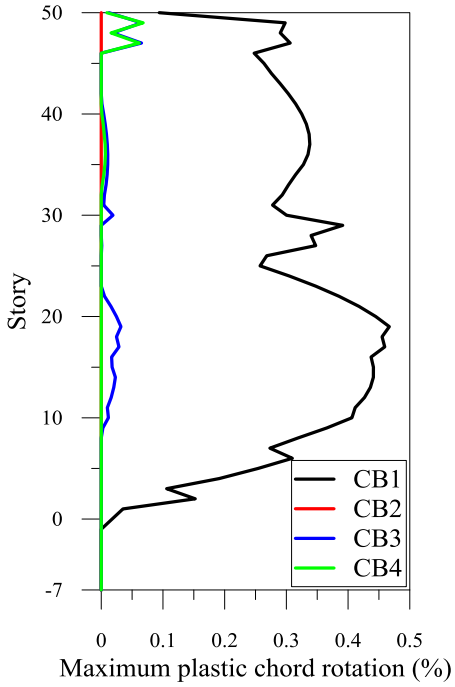

(b) Maximum plastic rotation of coupling beams

Figure 6-16 Response spectrum and maximum plastic rotation of MCE EQ5

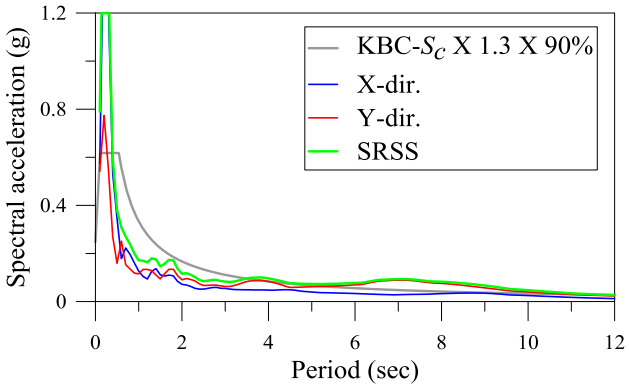

(a) Response spectrum

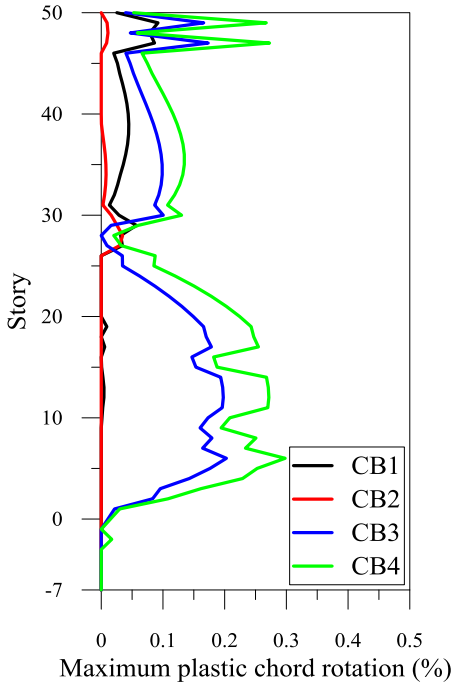

(b) Maximum plastic rotation of coupling beams

Figure 6-17 Response spectrum and maximum plastic rotation of MCE EQ6

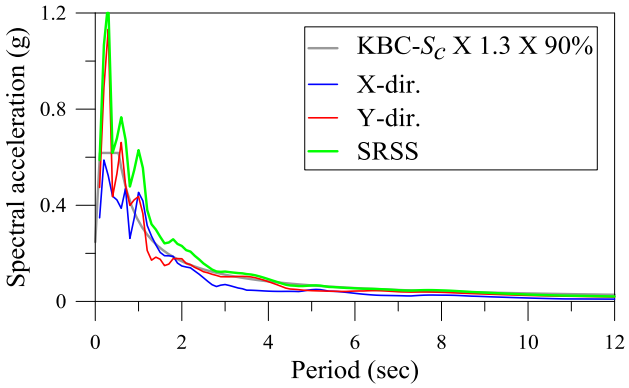

(a) Response spectrum

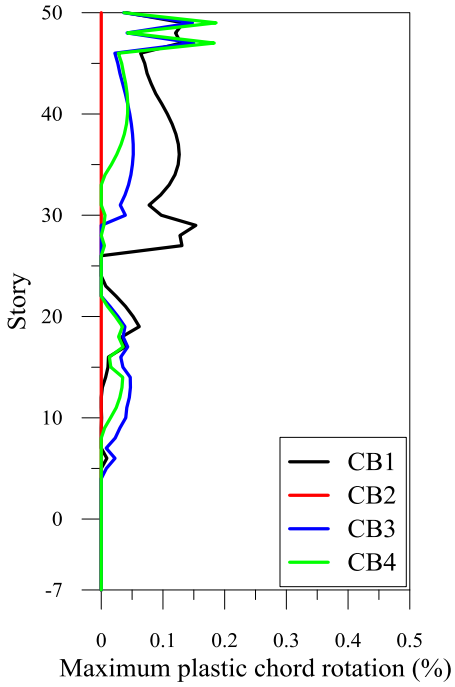

(b) Maximum plastic rotation of coupling beams

Figure 6-18 Response spectrum and maximum plastic rotation of MCE EQ7

6.7 Comparisons with the nonlinear static analysis

A large difference exists between the results of nonlinear static and dynamic analyses. The target displacement determined by the coefficient method in ASCE 41-13 or the performance point determined by the capacity spectrum method based on the equivalent linearization in FEMA 440 does not seem to predict the seismic performance of a high-rise building well, especially for a high-rise building with an asymmetric plan. The main limitation of nonlinear static analysis procedure is that a pushover analysis is conducted using the 1st mode load distribution. For a high-rise building, the influences of higher order modes are relatively larger than a mid-to-low-rise building. A pushover analysis using the 1st mode load distribution does not take into account the real collapse mechanism of the building. For the building studied here, the pushover curve of X-direction shows that the CB2 coupling beams yield prior to others and the plastic deformations are concentrated at the CB2 coupling beams. However, the results of the nonlinear time history analysis show that the plastic deformations mainly occur at the CB1 coupling beams. Such differences are mainly from the influence of the 3rd mode, the torsional mode. Thus, the accurate prediction of the target displacement or the performance point in nonlinear static analysis may not be reliable for asymmetric tall building analysis.

As a building with an asymmetric building, torsion can be one of the most governing modes. Because most of pushover analyses are conducted using the displacement control method to confirm the degradation of strength, it is hard to use torsional mode in a pushover analysis. ASCE 41-13 suggests that the monitored node at the roof be the center of mass, and the snap-back of the monitored node commonly occurs when a torsional mode pushover analysis is conducted. For this reason and other aforementioned reasons, nonlinear static analysis would not be recommended, if a tall building has an asymmetric plan.

In the coefficient method suggested by ASCE 41-13, there are four parameters

of C_0, C_1, C_2, T_e which can be determined by the characteristics of the building. The C_0 is the modification factor for the conversion of the roof displacement of the MDOF system to spectral displacement of SDOF. The C_1 is the factor to account for the expected maximum inelastic displacement. The C_2 is the factor to account for increase of displacement due to hysteretic behavior. And T_e is the effective period of the building. There is no parameter to control the damping ratio in the coefficient method, and it is difficult to know whether the C_0 properly reflects the influence of higher order modes of a high-rise building, because ASCE 41-13 suggests the same value of C_0 for the buildings with more than 10 stories. Furthermore, in the coefficient method, it is assumed that the inelastic displacement and elastic displacement are almost the same in a building with a long fundamental period. ASCE 41-13 suggests the values of C_1 and C_2 as 1.0 for a long period structure. However, the inelastic displacement of a high-rise building can also be larger under MCE. Due to the absence of a parameter to control the damping for a high-rise building and the potential for underestimation of inelastic displacement of a long period building, the target displacement determined by ASCE 41-13 is smaller than the results of the time history analyses in this study.

6.8 Discussion

In this chapter, a series of nonlinear time history analyses are conducted for both DBE and MCE. The influence of the basement modeling methods is compared. The seismic performance evaluations are also conducted and compared to those of nonlinear static analysis. The main results are summarized as follows:

1) From the nonlinear time history analysis, the seismic performance in term of interstory drift is turned out to be LS for DBE and CP for MCE. Only the coupling beams yield under both the DBE and MCE, and the maximum plastic rotation is less than 0.5% which is the performance level of IO in accordance with ASCE 41-13.

2) The results above the ground level are similar regardless of the basement modeling methods. However, the results below the ground level are very sensitive. An excessive shear force is observed at the $B1^{th}$ floor in the laterally supported model. The results of the comparison model including surrounding parking lot without the soil-structure-interaction would be closer to the actual behavior at the basement. However, computational cost is quite large to make the model and run the analysis. Although an exact modeling is recommended, considering the computational efforts, laterally supported model with the portion of the surrounding basement structures appears to be a proper method in design practice.

3) The responses of time history analysis is significantly sensitive to the characteristics of the input ground motions. The responses are largely affected by the magnitude of spectral acceleration near the periods of the 1^{st} to 3^{rd} modes in the response spectrum of each ground motion. Especially, the influence of the 3^{rd} mode, the torsional mode, is sensitive due to the use of Rayleigh damping.

4) The strong high-frequency components of a ground motion lead to the large plastic rotation of coupling beams at the upper parts of the building and the strong low-frequency components induce the large plastic rotation at the lower parts.

5) The nonlinear static analysis using the 1st mode load distribution may not take into consideration the collapse mechanism of the high-rise building. Because the seismic performance evaluation is conducted based on the pushover curve, the target displacement or performance point may not represent the actual behavior. It is difficult to account for the torsional mode in the pushover analysis, the nonlinear static analysis is not recommended for a building with an asymmetric plan and possibly a high-rise building governed by the higher order modes.

6) The coefficient method in ASCE 41-13 has limitations of no parameters to control the damping ratio of a building and potentially underestimate inelastic displacement of long period buildings. These limitations appear to make the target displacement smaller than the results of the time history analysis.

Chapter 7. Conclusion

In this study, seismic performance evaluation of a 49-story T-shape building is conducted using nonlinear static and nonlinear time history analysis. The conclusions are summarized as follows:

1) The inelastic behavior of a building is assumed in the seismic design code, and the seismic load is reduced by strength reduction factor. In order to assess such inelastic behavior and related loads, the seismic performance evaluation using nonlinear analysis is required, although a high-rise building is generally governed by wind loads.

2) For the high-rise building with core walls, the coupling beams are expected to yield prior to all the vertical members due to the relatively short span, so the accurate nonlinear modeling of coupling beams is very important.

3) The pivot hinge hysteresis model is proper to capture the hysteretic behavior of the coupling beam. The pivot point, β, is affected by the longitudinal reinforcement ratio and span-to-depth ratio of the coupling beam. In the pivot hysteresis model, the α and η of 3 and 0.1, respectively, can be used for general RC coupling beams.

4) The fundamental mode and 2^{nd} mode of one direction are recommended for two target modes as target damping ratio in the Rayleigh damping. The use of higher order modes for the target mode would underestimate the damping of governing modes.

5) According to the nonlinear static analysis, the coupling beams yield prior to the vertical members. The plastic deformations are concentrated at the CB2 coupling beams in the X-direction pushover and at the CB3 and CB4 in the Y-direction pushover.

6) The seismic performance evaluation is conducted by using the coefficient method of ASCE 41-13. The building remains almost elastic at the DBE target displacement. The yielding of CB2 coupling beams mainly occur at the MCE target displacement, but the plastic rotation is insignificant. All the vertical members are not subject to nonlinear deformations. Based on the interstory drifts, the seismic performance is LS at the DBE target displacement and CP at the MCE target displacement.

7) The maximum displacement during the nonlinear time history analysis is larger than the target displacement of the nonlinear static analysis. The yield range of the coupling beam is also larger for the results of the nonlinear time history analysis. Although there is some discrepancy, the seismic performance evaluation is the same as that of the nonlinear static analysis.

8) According to the nonlinear dynamic analysis, the critical member would be the CB1 coupling beam, which differs from the result of nonlinear static analysis. It is related to the influence of the higher order modes in the time history analysis. The nonlinear static analysis based on the 1^{st} mode load distribution may not take into consideration the collapse mechanism of a high-rise building. Because the seismic performance evaluation is conducted based on the pushover curve, the accuracy of the target displacement or performance point may be lower. It is difficult to consider the torsional mode in the pushover analysis, thus, the nonlinear static analysis is not recommended for a building with an asymmetric plan and a high-rise building governed by higher order modes.

9) The responses at the underground are sensitive to the basement modeling methods. The laterally supported model may overestimate the backstay effect, and underestimate the plastic deformation of the

underground structures. The comparison model including the surrounding parking lot without soil-structure-interaction would be closer to the actual condition, but large computational cost is required. The laterally supported model with the portion of the basement turns out to be more proper in actual design.

10) The responses of time history analysis are significantly sensitive to the characteristics of the input ground motions. The responses are largely affected by the magnitude of spectral acceleration near the periods of the 1^{st} to 3^{rd} modes in the response spectrum of each ground motion. Especially, the influence of the 3^{rd} mode, the torsional mode, is sensitive when using the Rayleigh damping.

References

1. American Society of Civil Engineers (ASCE) (2014), Seismic Evaluation and Retrofit of Existing Buildings (ASCE 41-13), Reston, VA.

2. Architectural Institute of Korea (2015), Guidelines for Performance-Based Seismic Design of Residential Buildings. (in Korean)

3. Broderick, B. M., Elnashai, A. S., and Izzuddin, B. A. (1994), "Observations on the effect of numerical dissipation on the nonlinear dynamic response of structural systems," Engineering Structures, Vol. 16, No. 1, pp. 51-62.

4. Computers & Structures, Inc. (CSi) (2016), CSi Analysis Reference Manual.

5. Dowell, R.K., Seible, F., and Wilson, E.L. (1998), "Pivot Hysteresis Model for Reinforced Concrete Members," ACI Structural Jornal, V. 95, No. 5, pp. 607-617.

6. Federal Emergency Management Agency (FEMA) (2000), Prestandard and Commentary for the Seismic Rehabilitation of Buildings (FEMA 356), prepared by the American Society of Civil Engineers for the Federal Emergency Management Agency, Washington, DC.

7. Federal Emergency Management Agency (FEMA) (2005), Improvement of nonlinear static seismic analysis procedures (FEMA 440), prepared by the Applied Technology Council for the Federal Emergency Management Agency, Washington, DC.

8. Galano, L. and Vignoli, A. (2000), "Seismic Behavior of Short Coupling Beams with Different Reinforcement Layouts," ACI Structural Jornal, V. 97, No. 6, pp. 876-885.

9. Kang, T.H.-K. and Wallace, J.W. (2005), "Dynamic Responses of Flat Plate Systems with Shear Reinforcement," ACI Structural Journal, V. 102, No. 5, pp. 763-773.

10. Korea Concrete Instituite (KCI) (2012), Concrete Design Code of Korea (KCI 2012). (in Korean)

11. Lequesne, R.D., Parra-Montesinos, G.J., and Wight, J.K. (2016), "Seismic Response of Fiber-Reinforced Concrete Coupled Walls," ACI Structural Journal, V. 113, No. 3, pp. 435-445.

12. Lim, E., Hwang, S.-J., Wang, T.-W., and Chang, Y.-H. (2016), "An

Investigation on the Seismic Behavior of Deep Reinforced Concrete Coupling Bemas," ACI Structural Jornal, V. 113, No. 2, pp. 217-226.

13. Lim, E., Hwang, S.-J., Cheng, C.-H., and Lin, P.-Y. (2016), "Cyclic Tests of Reinforced Concrete Coupling Beam with Intermediate Span-Depth Ratio," ACI Structural Jornal, V. 113, No. 3, pp. 515-524.

14. Ministry of Land, Infrastructure, and Transport (Korea) (2016), Korean Building Code (KBC 2016). (in Korean)

15. Naish, D., Fry, A., Klemencic, R., and Wallace J. (2013), "Reinforced Concrete Coupling Beams-Part I: Testing," ACI Structural Jornal, V. 110, No. 6, pp. 1057-1066.

16. PEER/ATC (2010), Modeling and Acceptance Criteria for Seismic Design and Analysis of Tall Buildings (PEER/ATC 72-1), Applied Technology Council, Redwood City, CA.

17. Tocci, N. and Levi, S. (2012), "Basement Modeling in Tall Buildings – Backstay Effect," Structure Magazine.

18. Popovics, S. (1973), "A Numerical Approach to the Complete Stress-Strain Curve of Concrete," Cement and Concrete Research, Vol. 3, No. 5, pp. 553-599.

19. Xiao, Y., Esmaeily-Ghasemabadi, A., and Wu, H. (1999), "High-Strength Concrete Short Beams Subjected to Cyclic Shear," ACI Structural Jornal, V. 96, No. 3, pp. 392-400.

국 문 초 록

비선형 해석을 통한 초고층 건물의 내진성능 평가

코어월 시스템은 초고층 건물의 횡력저항 요소로 흔히 활용되며, 코어의 개구부로 인해 연결보로 연결된 병렬 전단벽이 주로 사용된다. 일반적으로 연결보는 벽체에 비해 약하게 설계되기 때문에 지진하중이 작용할 때 전단벽보다 먼저 항복을 하게 된다. 따라서 연결보의 이력거동은 초고층 건물의 에너지 소산능력에 큰 영향을 주며, 초고층 건물의 내진해석 시 정확한 이력거동 모델링이 요구된다. 이 연구에서는 초고층 건물의 내진성능평가에 앞서 연결보의 단면과 형상비에 따른 이력거동에 대한 연구를 수행하였다. 또한 비선형 정적 및 동적해석을 통하여 코어월 시스템이 사용된 초고층 건물의 내진성능평가를 수행하였으며, 비선형 동적해석은 각각 7 개의 DBE 와 MCE 수준의 지진파에 대해 해석을 수행하였다. 비선형 정적 및 동적해석에 따른 내진성능평가에 대한 비교, 초고층 건물의 지하층 모델링 방법에 따른 거동, 그리고 지진파의 특성에 따른 초고층 건물의 비선형 거동에 대해 연구하였다.

ASCE 41-13에서 제시하는 비선형 정적해석의 변위계수법은 비선형 동적해석에 비해 일반적으로 초고층 건물의 내진성능을 과대평가하는 것으로 나타났다. 지하층 모델링 방법에 따른 비선형 동적해석 결과, 지반면 상부에 대해서는 큰 차이는 없었지만 지반면 하부 거동에서는 모델링 방법에 따른 차이가 매우 크게 나타났다. 또한, 지진파의 응답스펙트럼의 특성에 따라 응답의 차이가 크게 발생하였으며, 고차모드의 영향으로 인해 비선형 정적해석 결과와 상이한 결과가 나타났다.

핵심용어: 내진성능, 초고층, 비선형 동적해석, 지하구조물, 연결보
학번: 2015-22850